

Resistive effects on helicity-wave current drive generated by Alfvén waves in tokamak plasmas

C. BRUMA, S. CUPERMAN and K. KOMOSHVILI

School of Physics and Astronomy, Raymond and Beverly Sackler, Faculty of Exact Sciences, Tel Aviv University, Tel Aviv 69978, Israel

(Received 22 July 1996)

This work is concerned with the investigation of *non-ideal* (resistive) MHD effects on the excitation of Alfvén waves by externally launched fast-mode waves, in simulated tokamak plasmas; both *continuum* range, CR ($\{\omega_{\text{Alf}}(r)\}_{\text{min}} < \omega < \{\omega_{\text{Alf}}(r)\}_{\text{max}}$) and *discrete* range, DR, where global Alfvén eigenmodes, GAEs ($\omega < \{\omega_{\text{Alf}}(r)\}_{\text{min}}$) exist, are considered. (Here, $\omega_{\text{Alf}}(r) \equiv \omega_{\text{Alf}}[n(r), B_0(r)]$ is an eigenfrequency of the shear Alfvén wave.) For this, a cylindrical current carrying plasma surrounded by a helical sheet-current antenna and situated inside a perfectly conducting shell is used. Toroidicity effects are simulated by adopting for the axial equilibrium magnetic field component a suitable radial profile; shear and finite relative poloidal magnetic field are properly accounted for. *A dielectric tensor appropriate to the physical conditions considered in this paper is derived and presented.* When the resistive wave equation is solved and the current drive by helicity injection, I_{CD}^{HI} , is calculated, the following illustrative results are found to hold. For CR, (i) the maximum power absorption as well the maximum helicity injection current drive *increase significantly with decreasing resistivity* (i.e. with increasing temperature); (ii) unlike the power absorption, which is a maximum at a frequency between the lower and the upper edge of the CR, the total current drive is a maximum at the lower edge, and decreases strongly with increasing frequency; (iii) the behaviour of the efficiency closely follows that of the current drive; (iv) the smaller the resistivity, the smaller is the radial distance from the axis ($x = 0$) of the maximum current-drive density. For DR, (i) the maximum power absorption in the discrete GAE case increases with decreasing resistivity even more strongly than in the CR case; (ii) unlike the CR case, the total helicity-injection current has, for almost all GAEs, a symmetric frequency dependence about the line centre; its maximum value as well as the efficiency increase strongly with decreasing resistivity; (iii) unlike the continuum case, the efficiency is almost constant over the entire width of the discrete-mode range; its value increases strongly with the GAE rank.

1. Introduction

Externally launched low-frequency waves may provide the additional, non-inductive, steady-state current drive necessary for the operation of tokamaks in reactor-relevant regimes. Ohkawa (1989) suggested that *circularly* polarized waves carry non-zero helicity $\langle \mathbf{A} \cdot \mathbf{B} \rangle$, where \mathbf{A} and \mathbf{B} are respectively the vector potential

and the magnetic field of the wave, and the brackets $\langle \cdot \rangle$ indicate averaging over a wave period; the current is due to the helicity injection. A full discussion of the *helicity-wave current drive* (HWCD) is given in, for example, Chan *et al.* (1990), Kirov *et al.* (1990), Tataronis and Moroz (1991), Fukuyama *et al.* (1993) and Elfimov *et al.* (1994).

Now, the resonant excitation of shear Alfvén waves by externally launched fast waves is considered to represent an efficient way of fusion-plasma heating (see e.g. Tataronis and Grossman 1973; Tataronis 1975; Hasegawa and Chen 1976; Taylor 1989; Mett and Tataronis 1990; Mett and Taylor 1992; Tsypin *et al.* 1995; Wang *et al.* 1995; Rauf and Tataronis 1996). Within ideal MHD, theoretical investigations of HWCD generation by shear Alfvén waves (SAW), resonantly excited by an external antenna, in simulated tokamak plasmas have been recently carried out by Cuperman *et al.* (1996) (for the continuum range – SAW-CR – and small aspect ratio $R/a = 1.3$) and by Komoshvili *et al.* (1997) (for discrete, global Alfvén eigenmodes – GAEs – situated in the frequency range $\omega < \{\omega_{\text{Alf}}(r)\}_{\text{min}}$, where $\omega_{\text{Alf}}(r)$ is an eigenfrequency of SAW-CR; $\omega = \omega_{\text{Alf}}(r)$ defines the location of the mode-conversion layer where the spatial Alfvén resonance occurs). In both cases, sets of the antenna's poloidal (m) and 'toroidal' (n) wavenumbers leading to significant positive (i.e. in the direction of the equilibrium current) current drive have been formed.

Now, to obtain a better description of the physics involved, one has to consider also dissipative effects (e.g. plasma resistivity). Two obvious reasons for this are as follows.

- (i) The normal-mode solutions in the continuum range possess logarithmic singularities, which appear at positions where their eigenfrequencies match the local Alfvén frequencies. Resistivity, even very small, would remove singularities and render the solutions regular.
- (ii) In the absence of dissipation (e.g. resistivity), the absorbed energy is not transferred to current drive and heat.

More general discussions of Alfvén-wave propagation in resistive non-uniform plasmas can be found, for example, in Mok and Einaudi (1985) and Einaudi and Mok (1985).

In this paper we investigate resistivity effects on helicity-wave current drive generated by spatially resonant Alfvén waves excited in 'simulated' tokamak plasmas. Thus we treat the case of a current-carrying cylindrical plasma (of radius a) with periodic boundary conditions at the ends; the plasma is surrounded by a helical sheet-current antenna of radius r_A and by a perfectly conducting wall of a radius r_W ($a < r_A < r_W$). *Toroidicity* effects are simulated by adopting for the axial magnetic field component a suitable radial profile; *shear* and *finite relative poloidal field* are properly accounted for.

The paper is organized as follows. In Sec. 2 the basic equations used are presented and the equilibrium magnetic field configuration simulating the toroidal tokamak plasma is obtained. In Sec. 3 general explicit expressions for the components of the dielectric tensor corresponding to this equilibrium are derived within the framework of a two-fluid (resistive) model. The relevant wave equation based on the results of Secs 2 and 3 is derived in Sec. 4, and the expressions for current drive and power absorption are formulated in Sec. 5. A brief summary of the numerical algorithm

used in the work is presented in Sec. 6. The results and their discussion are given in Sec. 7. A summary is given in Sec. 8.

2. Configuration and model equations

2.1. Configuration

We consider a current-carrying cylindrical plasma of radius a and length $2\pi R$, with periodic boundary conditions at the ends, surrounded by a helical sheet-current antenna of radius r_A and a perfectly conducting wall of radius r_w ($a < r_A < r_w$). In cylindrical coordinates, (r, θ, z) the equilibrium magnetic field is

$$\mathbf{B}_0(r) = B_{0z}(\hat{\mathbf{z}} + \delta\hat{\boldsymbol{\theta}}), \quad (1)$$

$$\delta(r) \equiv B_{0\theta}(r)/B_{0z}(r) < 1, \quad (2)$$

where $\hat{\mathbf{z}}$ and $\hat{\boldsymbol{\theta}}$ are unit vectors in the z and θ directions respectively. Obviously, this equilibrium state implies concentric cylindrical magnetic surfaces.

The antenna current density is taken as

$$\mathbf{j} = \mathbf{j}_A \delta_D(r - r_A) \exp[i(m\theta + k_z z - \omega t)], \quad (3)$$

$$\mathbf{j}_A = \left(\hat{\boldsymbol{\theta}} k_z - \hat{\mathbf{z}} \frac{m}{r_A} \right) J_0. \quad (4)$$

Here m and k_z represent poloidal and ‘toroidal’ (axial) wavenumbers, J_0 is half the amplitude of the total current and $\delta_D(\cdot)$ is the Dirac delta function.

2.2. Model equations

The two-fluid, inviscid model equations are (see e.g. Kulsrud 1983)

$$m_i n \frac{d\mathbf{v}_i}{dt} = -\nabla p_i + Z e n \left(\mathbf{E} + \frac{\mathbf{v}_i \times \mathbf{B}}{c} \right) - \mathbf{R}_{ei}, \quad (5)$$

$$m_e n \frac{d\mathbf{v}_e}{dt} = -\nabla p_e - e n \left(\mathbf{E} + \frac{\mathbf{v}_e \times \mathbf{B}}{c} \right) + \mathbf{R}_{ei}, \quad (6)$$

$$\nabla \times \mathbf{E} = -\frac{1}{c} \frac{\partial \mathbf{B}}{\partial t}, \quad (7)$$

$$\nabla \times \mathbf{B} = \frac{4\pi}{c} \mathbf{j} + \frac{1}{c} \frac{\partial \mathbf{E}}{\partial t}. \quad (8)$$

Here $n = n_i = n_e$ is the particle number density; m_i (m_e) and p_i (p_e) are the ion (electron) mass, velocity and thermal pressure respectively; \mathbf{R}_{ei} is the rate of transfer of momentum from ions to electrons by collisions. In what follows, we take the ion charge $Z = 1$.

Using standard procedures, we obtain from (5) and (6) the following one-fluid and generalized Ohm’s equations respectively:

$$m_i n \frac{d\mathbf{V}}{dt} = -\nabla p + \frac{\mathbf{j} \times \mathbf{B}}{c}, \quad (9)$$

$$\left(\nu_{ei} + \frac{d}{dt} \right) \mathbf{j} = \frac{e}{m_e} \nabla p_e + \frac{ne^2}{m_e} \left[\mathbf{E} + \frac{1}{c} \left(\mathbf{V} - \frac{\mathbf{j}}{ne} \right) \times \mathbf{B} \right] - (\mathcal{P} - 1) \nu_{ei} \mathbf{j}_{\parallel}. \quad (10)$$

In these equations, the following notation is used:

$$\mathbf{V} \equiv \frac{m_i \mathbf{v}_i + m_e \mathbf{v}_e}{m_i + m_e}, \quad \mathbf{j} \equiv ne(\mathbf{v}_i - \mathbf{v}_e), \quad p \equiv p_i + p_e. \quad (11)$$

For \mathbf{R}_{ei} we use the expression (see e.g. Kulsrud, 1983)

$$\mathbf{R}_{ei} \equiv ne \left(\frac{\mathbf{j}_{\parallel}}{\sigma_{\parallel}} + \frac{\mathbf{j}_{\perp B}}{\sigma_{\perp}} \right), \quad (12)$$

$$\sigma_{\perp} \equiv \frac{ne^2}{m_e \nu_{ei}}, \quad \sigma_{\parallel} = 1.96 \sigma_{\perp}. \quad (13)$$

Here σ_{\perp} and σ_{\parallel} are the electrical conductivities in the directions respectively parallel (\parallel) and perpendicular (\perp) to the equilibrium magnetic field \mathbf{B}_0 ; the average electron-ion collision term is (see e.g. Braginskii 1964)

$$\nu_{ei}^{-1} = \frac{3}{4(2\pi)^{1/2}} \frac{m_e^{1/2} T_e^{3/2}}{ne^4 \Lambda}, \quad (14)$$

$$\Lambda = \begin{cases} 23.4 - 1.15 \log n + 3.45 \log T_e & (T_e < 50 \text{ eV}), \\ 25.3 - 1.15 \log n + 2.3 \log T_e & (T_e > 50 \text{ eV}), \end{cases} \quad (15)$$

where Λ is the Coulomb logarithm and T_e in (15) has to be expressed in eV; the other quantities are in Gaussian units. In (12), \mathbf{j}_{\parallel} and $\mathbf{j}_{\perp B}$ are the currents respectively parallel and perpendicular to \mathbf{B}_0 ; $\mathbf{j}_{\perp B}$ includes both the normal (to the magnetic surface) component and the binormal (transversal, \perp) component:

$$\mathbf{j}_{\perp B} = \mathbf{j}_N + \mathbf{j}_{\perp}. \quad (16)$$

Thus, with the notation $\mathcal{P} \equiv \sigma_{\perp}/\sigma_{\parallel} = 1/1.96$, (12) can be rewritten as

$$\mathbf{R}_{ei} = \frac{m_e \nu_{ei}}{e} [\mathbf{j} + (\mathcal{P} - 1)\mathbf{j}_{\parallel}], \quad (17)$$

where ν_{ei} is the electron-ion collision frequency.

In the derivation of (9) and (10), the following reasonable approximations have been used:

- (i) neglect of electron inertia in (11) leading to $\mathbf{V} \approx \mathbf{v}_i$;
- (ii) $T_{e0} \approx T_{i0}$, leading to the result $p_i/m_i - p_e/m_e \approx -p_e/m_e$.

Equations (9) and (10) are easily recognized as the *one-fluid motion equation* and the *generalized Ohm's law* respectively.

2.3. Equilibrium magnetic fields

For the case considered in this paper, namely $\mathbf{B}_0 = B_0(0, B_{0\theta}, B_{0z})$ and $\partial/\partial\theta = \partial/\partial z = 0$, and assuming $V_0 = 0$, from the force-balance equation we obtain the following equilibrium relations:

$$\frac{\partial p_0}{\partial r} = \frac{1}{c} j_{0\perp} B_0, \quad (18)$$

$$0 = \frac{1}{c} j_{0N} B_0. \quad (19)$$

Also, $j_{0\perp}$ can be expressed as

$$j_{0\perp} = b_z j_{0\theta} - b_{\theta} j_{0z} \quad (20)$$

($b_i(x) \equiv B_{0i}(x)/B_0(x)$, $i = \theta, z$).

The θ and z projections of the Ampère equation (8) provide

$$j_{0\theta} = -\frac{c}{4\pi} \frac{\partial B_{0z}}{\partial r}, \quad (21)$$

$$j_{0z} = \frac{c}{4\pi} \frac{1}{r} \frac{\partial}{\partial r} (r B_{0\theta}). \quad (22)$$

Substitution of the expressions for $j_{0\theta}$ and j_{0z} into (20) gives

$$j_{0\perp} = -\frac{c}{4\pi} \left[b_z \frac{\partial B_{0z}}{\partial r} + b_\theta \frac{1}{r} \frac{\partial}{\partial r} (r B_{0\theta}) \right]. \quad (23)$$

Finally, by (23), we can bring (18) into the form

$$\frac{\partial}{\partial r} \left(p_0 + \frac{B_{0\theta}^2 + B_{0z}^2}{8\pi} \right) = -\frac{B_{0\theta}^2}{4\pi r}. \quad (24)$$

Obviously, the actual r dependence of B_{0z} and $B_{0\theta}$ is determined – via Ampère's equation – by the equilibrium current \mathbf{j}_0 . For convenience, we here assume a quite general form for $j_{0z}(r)$, namely

$$j_{0z}(r) = j_{0z}(0) \left[1 - \left(\frac{r}{a} \right)^2 \right]^\nu, \quad (25)$$

where $j_{0z}(0)$ represents the current value at the plasma centre ($r = 0$) and $\nu \geq 1$.

Now, integration of (22) provides the following expression for $B_{0\theta}$ ($x \equiv r/a$):

$$B_{0\theta}(x) = B_{0\theta}(1) [1 - (1 - x^2)^{\nu+1}] / x, \quad (26)$$

where

$$B_{0\theta}(1) \equiv \frac{2\pi a}{c(\nu+1)} j_{0z}(0). \quad (27)$$

Next, integration of (24), with $B_{0\theta}(x)$ given by (26), provides, after some algebra, the following expression for $B_{0z}(x)$:

$$B_{0z}^2(x) = B_{0z}^2(0) + 8\pi[p_0(0) - p_0(x)] + 2(\nu+1)B_{0\theta}^2(1) \sum_{n=0}^{\nu} \frac{(1-x^2)^{n+\nu+1} - 1}{(n+\nu+1)}. \quad (28)$$

In the particular case $\nu = 2$ considered here, (25), (26) and (27) read respectively

$$j_{0z}(x) = j_{0z}(0) (1 - x^2)^2, \quad (29)$$

$$B_{0\theta}(x) = B_{0\theta}(1) x(3 - 3x^2 + x^4), \quad (30)$$

$$B_{0z}^2(x) = B_{0z}^2(0) + 8\pi[p_0(0) - p_0(x)] + 0.1 B_{0\theta}^2(1) [(1-x^2)^3(47 - 39x^2 + 12x^4) - 47]. \quad (31)$$

Finally, with the definitions

$$p_0 \equiv n_0(x)T_0(x), \quad (32)$$

$$\alpha \equiv B_{0\theta}(1)/B_{0z}(0), \quad (33)$$

$$\beta(x) \equiv 8\pi p_0(x)/B_{0z}^2(x), \quad (34)$$

we can rewrite (30) and (31) respectively as

$$\frac{B_{0\theta}(x)}{B_{0z}(0)} = \alpha x(3 - 3x^2 + x^4), \quad (35)$$

$$\left[\frac{B_{0z}(x)}{B_{0z}(0)} \right]^2 = 1 + \beta(0) - \beta(x) + \frac{1}{10} \alpha^2 [(1-x^2)^3 (47 - 39x^2 + 12x^4) - 47]. \quad (36)$$

For illustration, we choose

$$n_0(x) = n_0(0) (1 - \beta_n x^2), \quad \beta_n = 0.99, \quad (37)$$

$$T(x) = T(0) (1 - \beta_T x^2), \quad \beta_T = 0.75. \quad (38)$$

Then (36) reads

$$\begin{aligned} \left[\frac{B_{0z}(x)}{B_{0z}(0)} \right]^2 &= 1 + x^2 \beta(0) [(0.99 + 0.75) - 0.99 \cdot 0.75 x^2] \\ &\quad - \alpha^2 x^2 (18 - 27x^2 + 20x^4 - 7.5x^6 + 1.2x^8). \end{aligned} \quad (39)$$

Thus (35) and (39) represent a set of exact, consistent equations describing the equilibrium state.

At this point, the following remarks are in order. In some earlier works devoted to large-aspect-ratio tokamaks, B_{0z} was considered to be r -independent (see e.g. Appert and Václavík 1983; Ross *et al.* 1982). In Cuperman *et al.* (1996) the radial profile $B_{0z}(x)/B_{0z}(0) = (1 + \epsilon x)^{-1}$ was used, ϵ representing the inverse of the aspect ratio. Here we remove this assumption by taking advantage of the consistent solution found for B_{0z} , (39). First, noting that the equilibrium state is determined by the parameters $T(0)$, $n(0)$, $B(0)$ and α , and moreover that both $T(0)$ and $n(0)$ enter the expression for $\beta(0)$, it follows that the equilibrium is completely determined by $\beta(0)$ and α . Then, fixing these quantities, we define an equivalent ϵ value, $\epsilon_{\text{eq}} \equiv a/R$ (where R is the major radius) by requiring at $x = 1$ the condition

$$\left(\frac{1}{1 + \epsilon_{\text{eq}}} \right)^2 = 1 + \beta(0) [(\beta_n + \beta_T) - \beta_n \beta_T] - \alpha^2 (18 - 27 + 20 - 7.5 + 1.2),$$

where use of (39) has been made. This provides a close relation between ϵ_{eq} , $\beta(0)$ and α , namely

$$\epsilon_{\text{eq}} = \{1 + \beta(0) [(\beta_n + \beta_T) - \beta_n \beta_T] - 4.7\alpha^2\}^{-1/2} - 1.$$

3. Dielectric tensor operator

Linearization of (9) and (10) and neglect of pressure perturbations provides the following results (we have used here the notation $n = n_0 + n^{(1)}$, $\mathbf{V} = \mathbf{V}^{(1)}$, $\mathbf{E} = \mathbf{E}^{(1)}$, $\mathbf{B} = \mathbf{B}_0 + \mathbf{B}^{(1)}$ and $\mathbf{j} = \mathbf{j}_0 + \mathbf{j}^{(1)}$, and in what follows, for simplicity, have omitted the superscript (1)):

$$\frac{d\mathbf{V}}{dt} = \frac{\mathbf{j} \times \mathbf{B}_0 + \mathbf{j}_0 \times \mathbf{B}}{n_0 m_i c}, \quad (40)$$

$$\left(\frac{1}{\tau_e} + \frac{d}{dt} \right) \mathbf{j} = \frac{n_0 e^2}{m_e} \left(\mathbf{E} + \frac{\mathbf{V} \times \mathbf{B}_0}{c} - \frac{\mathbf{j} \times \mathbf{B}_0 + \mathbf{j}_0 \times \mathbf{B}}{n_0 e c} \right) - \frac{\mathcal{P} - 1}{\tau_e} \mathbf{j}_{\parallel}. \quad (41)$$

Thus (40) and (41) describe small electromagnetic perturbations.

3.1. Coordinate systems

In the following, two orthogonal coordinate systems are used:

- (i) *cylindrical (C)*: (r, θ, z) ;

(ii) *local-magnetic (LM)*: $(x_N, x_\perp, x_\parallel)$, with

$$(\nabla \times \mathbf{E})_N = \frac{\partial E_\parallel}{\partial x_\perp} - \frac{\partial E_\perp}{\partial x_\parallel}, \tag{42}$$

$$(\nabla \times \mathbf{E})_\perp = \frac{\partial E_N}{\partial x_\parallel} - \frac{\partial E_\parallel}{\partial x_N} + \frac{1}{1 + \delta^2} \left[r \left(\frac{\delta}{r} \right)' E_\perp - \frac{\delta^2}{r} E_\parallel \right], \tag{43}$$

$$(\nabla \times \mathbf{E})_\parallel = \frac{1}{r} \frac{\partial}{\partial x_N} (r E_\perp) - \frac{\partial E_N}{\partial x_\perp} - \frac{1}{1 + \delta^2} \left[\frac{\delta^2}{r} E_\perp - \frac{(r\delta)'}{r} E_\parallel \right]. \tag{44}$$

Here the prime stands for d/dr , and $\delta(r)$ is defined by (2).

The following expressions relating components in the two systems of coordinates hold:

$$\begin{aligned} E_N &= E_r, \\ E_\perp &= b_z E_\theta - b_\theta E_z, & E_\theta &= b_z E_\perp + b_\theta E_\parallel, \\ E_\parallel &= b_\theta E_\theta + b_z E_z, & E_z &= -b_\theta E_\perp + b_z E_\parallel. \end{aligned}$$

Finally, the unit vectors of the local-magnetic coordinate system are

$$\hat{\mathbf{e}}_N \equiv \hat{\mathbf{e}}_r, \quad \hat{\mathbf{e}}_\perp \equiv \hat{\mathbf{e}}_\parallel \times \hat{\mathbf{e}}_N, \quad \hat{\mathbf{e}}_\parallel \equiv \frac{\mathbf{B}_0}{B_0}. \tag{45}$$

3.2. Derivation of the conductivity tensor

The calculation of the elements of the dielectric tensor requires first that of the elements of the conductivity tensor defined by the relation

$$\mathbf{j} = \boldsymbol{\sigma} \cdot \mathbf{E}. \tag{46}$$

To proceed, we assume that the perturbations can be described by Fourier-type single harmonics:

$$\mathbf{V}, \mathbf{j}, \mathbf{E}, \mathbf{B} \propto \exp[i(k_z z + m\theta - \omega t)]. \tag{47}$$

Then (40) and (41) take the respective forms

$$\mathbf{V} = -\frac{\mathbf{j} \times \mathbf{B}_0 + \mathbf{j}_0 \times \mathbf{B}}{i\omega n_0 m_i c}, \tag{48}$$

$$(\nu_{ei} - i\omega)\mathbf{j} = \frac{n_0 e^2}{m_e} \left(\mathbf{E} - \frac{\mathbf{j} \times \mathbf{B}_0 + \mathbf{j}_0 \times \mathbf{B}}{i\omega n_0 m_i c^2} \times \mathbf{B}_0 - \frac{\mathbf{j} \times \mathbf{B}_0 + \mathbf{j}_0 \times \mathbf{B}}{n_0 e c} \right) - (\mathcal{P} - 1)\nu_{ei}\mathbf{j}_\parallel. \tag{49}$$

To obtain (49), we have used (48) as well as the notation $\nu_{ei} \equiv 1/\tau_e$.

Now, in LM coordinates, we have $\mathbf{b} \equiv \mathbf{B}_0/B_0 = (0, 0, 1)$. Thus the following relations hold:

$$(\mathbf{j} \times \mathbf{b})_N = j_\perp, \quad (\mathbf{j} \times \mathbf{b})_\perp = -j_N, \quad (\mathbf{j} \times \mathbf{b})_\parallel = 0, \tag{50}$$

$$[(\mathbf{j} \times \mathbf{b}) \times \mathbf{b}]_N = (\mathbf{j} \times \mathbf{b})_\perp = -j_N, \tag{51}$$

$$[(\mathbf{j} \times \mathbf{b}) \times \mathbf{b}]_\perp = -(\mathbf{j} \times \mathbf{b})_N = -j_\perp, \tag{52}$$

$$[(\mathbf{j} \times \mathbf{b}) \times \mathbf{b}]_\parallel = 0. \tag{53}$$

With these relations, and using also the notation $\Gamma \equiv (\nu_{ei} - i\omega)/\omega_{ce}$, (49) can be

written as

$$\Gamma \mathbf{j} = \frac{n_0 ec}{B_0} \mathbf{E} - \mathbf{M} - (\mathcal{P} - 1) \left(\Gamma + \frac{i\omega}{\omega_{ce}} \right) \mathbf{j}_{\parallel}, \tag{54}$$

where

$$\mathbf{M} \equiv \frac{\omega_{ci}}{i\omega} \left(\frac{\mathbf{j}_0}{B_0} \times \mathbf{B} \right) \times \mathbf{b} + \frac{\mathbf{j}_0}{B_0} \times \mathbf{B}. \tag{55}$$

Projection of (54) onto the three directions of the LM coordinate system gives

$$\Gamma j_N - \frac{\omega_{ci}}{i\omega} j_N + j_{\perp} = \frac{n_0 ec}{B_0} E_N - M_N, \tag{56}$$

$$\Gamma j_{\perp} - \frac{\omega_{ci}}{i\omega} j_{\perp} - j_N = \frac{n_0 ec}{B_0} E_{\perp} - M_{\perp}, \tag{57}$$

$$\Gamma j_{\parallel} = \frac{n_0 ec}{B_0} E_{\parallel} - M_{\parallel} - (\mathcal{P} - 1) \left(\Gamma + \frac{i\omega}{\omega_{ce}} \right) j_{\parallel}. \tag{58}$$

Since (58) is independent of the previous two, we solve (56) and (57) for the components j_N and j_{\perp} . With the notation

$$\psi \equiv \Gamma - \frac{\omega_{ci}}{i\omega}, \quad \Delta \equiv 1 + \psi^2, \tag{59}$$

we obtain the solutions

$$j_N = \frac{1}{\Delta} \left[\psi \left(\frac{n_0 ec}{B_0} E_N - M_N \right) - \frac{n_0 ec}{B_0} E_{\perp} + M_{\perp} \right], \tag{60}$$

$$j_{\perp} = \frac{1}{\Delta} \left[\psi \left(\frac{n_0 ec}{B_0} E_{\perp} - M_{\perp} \right) + \frac{n_0 ec}{B_0} E_N - M_N \right]. \tag{61}$$

To obtain the components of \mathbf{M} , we first observe that the components of Faraday’s equation can be written as

$$\frac{i\omega}{c} B_N = (\nabla \times \mathbf{E})_N = ik_{\perp} E_{\parallel} - ik_{\parallel} E_{\perp}, \tag{62}$$

$$\frac{i\omega}{c} B_{\perp} = (\nabla \times \mathbf{E})_{\perp} = ik_{\parallel} E_N - E_{\parallel}' + \lambda E_{\perp} - \gamma E_{\parallel}, \tag{63}$$

$$\frac{i\omega}{c} B_{\parallel} = (\nabla \times \mathbf{E})_{\parallel} = -ik_{\perp} E_N + \frac{(rE_{\perp})'}{r} - \gamma E_{\perp} + \mu E_{\parallel}. \tag{64}$$

Here the following notation has been used:

$$\lambda \equiv \frac{r(\delta/r)'}{1 + \delta^2}, \quad \gamma \equiv \frac{\delta^2/r}{1 + \delta^2}, \quad \mu \equiv \frac{(r\delta)'/r}{1 + \delta^2}. \tag{65}$$

Secondly, we note that, with the notation $\mathbf{s} \equiv \mathbf{j}/B_0$, (55) reads

$$\mathbf{M} = \frac{\omega_{ci}}{i\omega} (\mathbf{s} \times \mathbf{B}) \times \mathbf{b} + \mathbf{s} \times \mathbf{B}. \tag{66}$$

Since $\mathbf{j}_0 = (0, j_{0\perp}, j_{0\parallel})$, it follows that

$$(\mathbf{s} \times \mathbf{B})_N = s_{\perp} B_{\parallel} - s_{\parallel} B_{\perp}, \quad (\mathbf{s} \times \mathbf{B})_{\perp} = s_{\parallel} B_N, \quad (\mathbf{s} \times \mathbf{B})_{\parallel} = -s_{\parallel} B_N, \tag{67}$$

$$[(\mathbf{s} \times \mathbf{B}) \times \mathbf{b}]_N = (\mathbf{s} \times \mathbf{B})_{\perp} = s_{\parallel} B_N, \tag{68}$$

$$[(\mathbf{s} \times \mathbf{B}) \times \mathbf{b}]_{\perp} = -(\mathbf{s} \times \mathbf{B})_N = s_{\parallel} B_{\perp} - s_{\perp} B_{\parallel}, \tag{69}$$

$$[(\mathbf{s} \times \mathbf{B}) \times \mathbf{b}]_{\parallel} = 0. \tag{70}$$

Combining (66)–(70) provides the following expressions for the components of \mathbf{M} :

$$M_N = \frac{\omega_{ci}}{i\omega} s_{\parallel} B_N + s_{\perp} B_{\parallel} - s_{\parallel} B_{\perp}, \quad (71)$$

$$M_{\perp} = \frac{\omega_{ci}}{i\omega} (s_{\parallel} B_{\perp} - s_{\perp} B_{\parallel}) + s_{\parallel} B_N, \quad (72)$$

$$M_{\parallel} = -s_{\perp} B_N. \quad (73)$$

Finally, substituting (62)–(64) into (71)–(73), we obtain

$$\begin{aligned} \frac{i\omega}{c} M_N = & -ik_s E_N + \left[s_{\perp} \check{D}_1 - s_{\parallel} \left(\lambda + \frac{\omega_{ci}}{i\omega} ik_{\parallel} \right) \right] E_{\perp} \\ & + \left[s_{\perp} \mu + s_{\parallel} \left(\check{D}_2 + \frac{\omega_{ci}}{i\omega} ik_{\perp} \right) \right] E_{\parallel}, \end{aligned} \quad (74)$$

$$\begin{aligned} \frac{i\omega}{c} M_{\perp} = & \frac{\omega_{ci}}{i\omega} ik_s E_N + \left[-\frac{\omega_{ci}}{i\omega} s_{\perp} \check{D}_1 + s_{\parallel} \left(\frac{\omega_{ci}}{i\omega} \lambda - ik_{\parallel} \right) \right] E_{\perp} \\ & + \left[-\frac{\omega_{ci}}{i\omega} s_{\perp} \mu - s_{\parallel} \left(\frac{\omega_{ci}}{i\omega} \check{D}_2 - ik_{\perp} \right) \right] E_{\parallel}, \end{aligned} \quad (75)$$

$$\frac{i\omega}{c} M_{\parallel} = is_{\perp} (k_{\parallel} E_{\perp} - k_{\perp} E_{\parallel}), \quad (76)$$

where

$$\check{D}_1 \equiv \partial_r + \frac{1}{r} - \gamma, \quad \check{D}_2 \equiv \partial_r + \gamma, \quad k_s \equiv ik_{\perp} s_{\perp} + ik_{\parallel} s_{\parallel}. \quad (77)$$

We are now in a position to give the RF current components, (60), (61) and (58). After some algebra, we obtain the following results:

$$\begin{aligned} \frac{j_N}{\mathcal{C}} = & (\epsilon_1 + K) E_N + (\epsilon_2 - K_{\perp} \check{D}_1 + K_{\parallel} \lambda - ik_{\parallel} K_{\parallel} \Theta) E_{\perp} \\ & + (-\mu K_{\perp} - K_{\parallel} \check{D}_2 + ik_{\perp} K_{\parallel} \Theta) E_{\parallel}, \end{aligned} \quad (78)$$

$$\begin{aligned} \frac{j_{\perp}}{\mathcal{C}} = & (-\epsilon_2 + K \Theta) E_N + (\epsilon_1 - K_{\perp} \Theta \check{D}_1 + K_{\parallel} \lambda \Theta + ik_{\parallel} K_{\parallel}) E_{\perp} \\ & + (-\mu K_{\perp} \Theta - K_{\parallel} \Theta \check{D}_2 - ik_{\perp} K_{\parallel}) E_{\parallel}, \end{aligned} \quad (79)$$

$$\frac{j_{\parallel}}{\mathcal{C}} = -ik_{\parallel} L_{\perp} E_{\perp} + (\epsilon_3 + ik_{\perp} L_{\perp}) E_{\parallel}, \quad (80)$$

with the notation

$$\left. \begin{aligned} \mathcal{C} & \equiv -\frac{i\omega}{4\pi} \left(\frac{c}{\omega} \right)^2, & K_{\perp, \parallel} & \equiv \frac{\Gamma}{\Delta} \frac{4\pi}{c} s_{\perp, \parallel}, \\ L_{\perp, \parallel} & \equiv \frac{4\pi}{c} \frac{s_{\perp, \parallel}}{\mathcal{P}(\Gamma + i\omega/\omega_{ce}) - i\omega/\omega_{ce}}, \\ K & \equiv ik_{\perp} K_{\perp} + ik_{\parallel} K_{\parallel}, & \Theta & \equiv \frac{1 - (\omega_{ci}/i\omega)\psi}{\Gamma}, \end{aligned} \right\} \quad (81)$$

$$\epsilon_1 \equiv \left(\frac{\omega}{c_A} \right)^2 \frac{1 - (i\omega/\omega_{ci})\Gamma}{[1 - (i\omega/\omega_{ci})\Gamma]^2 - (\omega/\omega_{ci})^2}, \quad (82)$$

$$\epsilon_2 \equiv \left(\frac{\omega}{c_A} \right)^2 \frac{i\omega/\omega_{ci}}{[1 - (i\omega/\omega_{ci})\Gamma]^2 - (\omega/\omega_{ci})^2}, \quad (83)$$

$$\epsilon_3 \equiv \frac{i\omega\omega_{ci}}{c_A^2} \left[\mathcal{P} \left(\Gamma + \frac{i\omega}{\omega_{ce}} \right) - \frac{\omega}{\omega_{ce}} \right]^{-1}. \quad (84)$$

Now, the elements of the conductivity tensor can be written as:

$$\sigma_{NN} = \mathcal{C}(\epsilon_1 + K), \quad (85)$$

$$\check{\sigma}_{N\perp} = \mathcal{C}(\epsilon_2 - K_{\perp}\check{D}_1 + K_{\parallel}\lambda - ik_{\parallel}K_{\parallel}\Theta), \quad (86)$$

$$\check{\sigma}_{N\parallel} = \mathcal{C}(-\mu K_{\perp} - K_{\parallel}\check{D}_2 + ik_{\perp}K_{\parallel}\Theta), \quad (87)$$

$$\sigma_{\perp N} = \mathcal{C}(-\epsilon_2 + K\Theta), \quad (88)$$

$$\check{\sigma}_{\perp\perp} = \mathcal{C}(\epsilon_1 - K_{\perp}\Theta\check{D}_1 + K_{\parallel}\lambda\Theta + ik_{\parallel}K_{\parallel}), \quad (89)$$

$$\check{\sigma}_{\perp\parallel} = \mathcal{C}(-\mu K_{\perp}\Theta - K_{\parallel}\Theta\check{D}_2 - ik_{\perp}K_{\parallel}), \quad (90)$$

$$\sigma_{\parallel N} = 0, \quad (91)$$

$$\sigma_{\parallel\perp} = \mathcal{C}(-ik_{\parallel}L_{\perp}), \quad (92)$$

$$\sigma_{\parallel\parallel} = \mathcal{C}(\epsilon_3 + ik_{\perp}L_{\perp}). \quad (93)$$

Here ‘ $\check{}$ ’ indicates that the tensor element contains the operation ∂_r .

Upon substituting (46) into Ampère’s law, we obtain

$$\nabla \times \mathbf{B} = \left(\frac{4\pi}{c} \boldsymbol{\sigma} - \frac{i\omega}{c} \mathbf{I} \right) \mathbf{E} = -\frac{i\omega}{c} \left(\mathbf{I} - \frac{4\pi}{i\omega} \boldsymbol{\sigma} \right) \mathbf{E}. \quad (94)$$

Therefore

$$\boldsymbol{\varepsilon} = \mathbf{I} - \frac{4\pi}{i\omega} \boldsymbol{\sigma}, \quad (95)$$

where $\boldsymbol{\varepsilon}$ is the dielectric tensor and \mathbf{I} is the unit tensor.

For convenience, we define

$$\mathcal{B} = \frac{i\omega}{c} \mathbf{B}. \quad (96)$$

Then multiplication of (94) by $i\omega/c$ leads to

$$\nabla \times \mathcal{B} = \boldsymbol{\varepsilon} \mathbf{E}, \quad (97)$$

where

$$\boldsymbol{\varepsilon} \equiv \left(\frac{\omega}{c} \right)^2 \boldsymbol{\varepsilon} = \left(\frac{\omega}{c} \right)^2 \mathbf{I} + \frac{\boldsymbol{\sigma}}{\mathcal{C}}. \quad (98)$$

Finally, making use of the elements of the conductivity tensor $\boldsymbol{\sigma}$ ((85)–(93)), we obtain the desired, explicit elements of the dielectric tensor $\boldsymbol{\varepsilon}$ as follows:

$$\epsilon_{NN} = \epsilon_1 + K + \left(\frac{\omega}{c} \right)^2, \quad (99)$$

$$\check{\epsilon}_{N\perp} = \epsilon_2 - K_{\perp}\check{D}_1 + K_{\parallel}(\lambda - ik_{\parallel}\Theta), \quad (100)$$

$$\check{\epsilon}_{N\parallel} = -\mu K_{\perp} - K_{\parallel}\check{D}_2 + ik_{\perp}K_{\parallel}\Theta, \quad (101)$$

$$\epsilon_{\perp N} = -\epsilon_2 + K\Theta, \quad (102)$$

$$\check{\epsilon}_{\perp\perp} = \epsilon_1 - K_{\perp}\Theta\check{D}_1 + K_{\parallel}(\lambda\Theta + ik_{\parallel}) + \left(\frac{\omega}{c} \right)^2, \quad (103)$$

$$\check{\epsilon}_{\perp\parallel} = -\mu K_{\perp}\Theta - K_{\parallel}(\Theta\check{D}_2 + ik_{\perp}), \quad (104)$$

$$\epsilon_{\parallel N} = 0, \quad (105)$$

$$\epsilon_{\parallel\perp} = -ik_{\parallel}L_{\perp}, \quad (106)$$

$$\epsilon_{\parallel\parallel} = \epsilon_3 + ik_{\perp}L_{\perp} + \left(\frac{\omega}{c} \right)^2. \quad (107)$$

4. The wave equation

We use the LM coordinates defined in Sec. 3.1. For the case $E_{\parallel} = 0$ considered here, utilizing standard procedures, from (7)–(10) and (99)–(107), after some lengthy algebra, we obtain the following wave equations for the RF-field components E_{\perp} and B_{\parallel} :

$$\mathcal{A} \frac{d}{dr} \begin{bmatrix} E_{\perp} \\ \mathcal{B}_{\parallel} \end{bmatrix} = \begin{bmatrix} a_{11} & a_{12} \\ a_{21} & a_{22} \end{bmatrix} \begin{bmatrix} E_{\perp} \\ \mathcal{B}_{\parallel} \end{bmatrix}, \quad (108)$$

where

$$a_{11} = k_{\perp} \mathcal{G} - \frac{b_z^2}{r} \mathcal{A}, \quad (109)$$

$$a_{12} = \mathcal{A} + ik_{\perp}(ik_{\perp} + K_{\perp}), \quad (110)$$

$$a_{21} = \mathcal{G}(\mathcal{G} + i\lambda K_{\parallel}) - \mathcal{A}[\mathcal{A} - \lambda(\lambda - \Theta K_{\parallel})], \quad (111)$$

$$a_{22} = (K_{\perp} + ik_{\perp})(i\mathcal{G} - \lambda K_{\parallel}) + \mathcal{A} \left(\Theta K_{\perp} - \frac{b_{\theta}^2}{r} \right). \quad (112)$$

The other field components are related to E_{\perp} and B_{\parallel} by the following algebraic relations:

$$\mathcal{B}_N = -ik_{\parallel} E_{\perp}, \quad (113)$$

$$\mathcal{A} E_N = -i\mathcal{G} E_{\perp} + (ik_{\perp} + K_{\perp}) \mathcal{B}_{\parallel}, \quad (114)$$

$$\mathcal{A} \mathcal{B}_{\perp} = (\lambda \mathcal{A} + k_{\parallel} \mathcal{G}) E_{\perp} + ik_{\parallel}(ik_{\perp} + K_{\perp}) \mathcal{B}_{\parallel}. \quad (115)$$

In (108)–(115) the following definitions have been used:

$$\mathcal{A} \equiv A - k_{\parallel}^2 + ik_{\parallel} K_{\parallel}, \quad (116)$$

$$A \equiv \left(\frac{\omega}{c} \right)^2 + \epsilon_1, \quad (117)$$

$$\mathcal{G} \equiv i[-\epsilon_2 + ik_{\parallel} \Theta K_{\parallel} - \lambda(K_{\parallel} + ik_{\parallel})]. \quad (118)$$

The quantities K_{\parallel} , K_{\perp} , Θ , ϵ_1 and ϵ_2 are defined in Sec. 3.2.

Note that in the limit of ideal MHD (zero resistivity), the (complex) quantity \mathcal{A} reduces to the quantity A , which is always real and characterizes the continuum range ($A = 0$) of the Alfvén wave. Thus we redefine here the continuum range by the condition $\text{Re } \mathcal{A} = 0$.

5. Current drive and power absorption

The electron current-drive (CD) density induced via helicity injection (HI), averaged over magnetic surfaces of a cylindrical plasma is given by (see e.g. Elfilimov *et al.* 1994)

$$\langle j_{CD}^{HI} \rangle = \frac{B_{0z}}{4\pi n \eta_{\parallel} B_0^2} \left\{ \frac{B_{0\theta}}{r^2} \frac{\partial}{\partial r} \left[r^2 \left(j_r^* \frac{E_{\theta}}{i\omega} \right) \right] + \frac{B_{0z}}{r} \frac{\partial}{\partial r} \left[r \left(j_r^* \frac{E_z}{i\omega} \right) \right] \right\} + \text{c.c.} \quad (119)$$

Here E_{θ} and E_z are respectively the θ and z components of the wave, j_r^* is the complex conjugate of the oscillatory radial plasma current, and η_{\parallel} is the electrical resistivity defined by the relation (see e.g. Braginskii 1964)

$$\eta_{\parallel} \equiv \frac{1}{\sigma_{\parallel}} = \frac{m_e \nu_{ei}}{1.96 n e^2}. \quad (120)$$

Using the normalizations

$$\left. \begin{aligned} \bar{\omega} &= \frac{\omega}{\omega_{ci}(0)}, & x &= \frac{r}{a}, & \bar{T} &= \frac{T}{T(0)}, & \bar{n} &= \frac{n}{n(0)}, \\ \bar{j} &= j \frac{4\pi a}{cB(0)}, & \bar{E} &= E \frac{c}{aB(0)\omega_{ci}(0)}, \end{aligned} \right\} \quad (121)$$

we may bring (119) to the form

$$\langle \bar{j}_{CD}^{HI} \rangle = \frac{C^{HI} \bar{T}^{3/2}}{\bar{\omega} \bar{n} \Lambda} b_z \left\{ \frac{b_\theta}{x^2} \frac{\partial}{\partial x} [x^2 \text{Im}(\bar{j}_r^* \bar{E}_\theta)] + \frac{b_z}{x} \frac{\partial}{\partial x} [x \text{Im}(\bar{j}_r^* \bar{E}_z)] \right\}, \quad (122)$$

where the constant C^{HI} is defined by

$$C^{HI} \equiv \frac{3 \times 1.96}{8c(2\pi)^{1/2}} \frac{B(0)T(0)^{3/2}}{n(0)e^3(m_e)^{1/2}}. \quad (123)$$

The total HWCD is

$$I_{CD}^{HI} = 2\pi \int_0^a \langle j_{CD}^{HI} \rangle r dr, \quad (124)$$

or, after some algebras,

$$\bar{I}_{CD}^{HI} = \frac{Q_0}{\bar{\omega}} \left\{ \int_0^1 V_1(x) \frac{dU_1(x)}{dx} dx + \int_0^1 V_2(x) \frac{dU_2(x)}{dx} dx \right\}, \quad (125)$$

where

$$\left. \begin{aligned} V_1(x) &\equiv \frac{\bar{T}^{3/2}}{\bar{n}\Lambda} \frac{b_z b_\theta}{x}, & U_1(x) &\equiv x^2 \text{Im}(\bar{j}_r^* \bar{E}_\theta), \\ V_2(x) &\equiv \frac{\bar{T}^{3/2}}{\bar{n}\Lambda} b_z^2, & U_2(x) &\equiv x \text{Im}(\bar{j}_r^* \bar{E}_z), \\ Q_0 &\equiv \frac{1}{2} caB(0)C^{HI}, & I &\equiv \frac{1}{2} caB(0)\bar{I}. \end{aligned} \right\} \quad (126)$$

Finally, integration by parts brings (125) to the form

$$\bar{I}_{CD}^{HI} = \frac{Q_0}{\bar{\omega}} \left[U_1(1)V_1(1) + U_2(1)V_2(1) - \int_0^1 U_1 \frac{dV_1}{dx} dx - \int_0^1 U_2 \frac{dV_2}{dx} dx \right]. \quad (127)$$

The current density \bar{j}_r^* appearing above is obtained from (46). In Sec. 7, where the calculation results are presented, the value \bar{I}_{CD}^{HI}/Q_0 is implied.

For the present configuration (a cylindrical plasma surrounded by a helical sheet-current antenna), the power per unit length absorbed by the plasma column is (see e.g. Appert and Václavík, 1983):

$$P = -\frac{1}{4} ac \text{Re}(E_\perp B_\parallel^*)_{r=a}. \quad (128)$$

With the normalizations used in this paper, (128) can be rewritten as

$$P = -P_0 \text{Re}(\bar{E}_\perp \bar{B}_\parallel^*)_{r=a} \equiv P_0 \bar{P}, \quad (129)$$

where $\bar{B} \equiv B/B(0)$ and

$$P_0 = \frac{1}{4} a^2 \omega_{ci}(0) B^2(0). \quad (130)$$

6. Numerical algorithm

The solution method employed in this work is based on a fourth-order Runge–Kutta algorithm with an adjustable grid size. In line with Villard *et al.* (1986) and

Cuperman *et al.* (1996), we solve (108) for the rf field components E_{\perp} and \mathcal{B}_{\parallel} , subject to the following boundary conditions:

- (i) at $r = 0$, regularity of the (plasma) solution;
- (ii) at $r = a$, the continuity of the plasma-vacuum solutions;
- (iii) at $r = r_A$, the requirement that the magnetic field components match those due to the surface currents in the antenna;
- (iv) at $r = r_w$, an infinitely conducting metallic wall ($\mathcal{B}_r(r_w) = 0$).

Full details are given in the references indicated above.

7. Results and discussion

For illustration, the following geometrical and physical parameters are considered here:

$$\begin{aligned} x_A \equiv \frac{r_A}{a} &= 1.2, & x_w \equiv \frac{r_w}{a} &= 1.5, & a &= 31 \text{ cm}, \\ B_{0z}(0) &= 1.0 \text{ T}, & n(0)T(0) &= 10^{16} \text{ eV cm}^{-3}, \\ m &= -1, & \bar{k}_z \equiv k_z a &= -0.3, & \alpha &= 0.2. \end{aligned}$$

For convenience, we analyse separately the *continuum* range of Alfvén waves (CR) ($\omega_{cL} \leq \omega \leq \omega_{cR}$) and the *discrete* range (DR) with global Alfvén eigenmodes (GAEs).

7.1. Continuum range

7.1.1. Frequency spectra. Some illustrative results of our investigations are represented in Figs 1(a–d). Thus, Figs 1(a–c) show respectively the frequency dependence of the total power absorption \bar{P} (128), the total current drive \bar{I}_{CD}^{HI} (125) and the efficiency $S \equiv \bar{I}_{CD}^{HI}/\bar{P}$ for electrical-resistivity values corresponding to temperatures $T_1 = 80 \text{ eV}$, $T_2 = 100 \text{ eV}$ and $T_3 = 120 \text{ eV}$. In Fig. 1(a), the labels on the curve $\bar{P}(T_2)$, namely † cL, c1 and cR indicate values corresponding to the lower edge frequency of CR, the main peak frequency and the upper edge frequency of CR respectively. (Similar frequency values – not indicated – do exist also for the curves $\bar{P}(T_1)$ and $\bar{P}(T_3)$.)

Inspection of Figs 1(a–c) indicates the following.

- (i) The maximum power absorption, as well as the corresponding normalized frequency values, increase almost linearly with the temperature (Fig. 1a).
- (ii) The maximum HI current drive increases almost linearly with the temperature, and, unlike the total power absorption, occurs at lower Alfvén frequency ω_{cL} . A very strong decrease with $\bar{\omega}$ after $\bar{\omega}_{cL}$ is apparent in each case (Fig. 1b).
- (iii) The efficiency behaviour follows closely that of the current drive (Fig. 1c).

For completeness, in Fig. 1(d) we plot the radial profile of $\text{Re } \mathcal{A}$ (\mathcal{A} is the coefficient of the derivative term in (108), see (116)). The meaning of the notation cL, c1 and

† For simplicity, we replace the notation $\{\omega_{\text{Alf}}\}_{\min}$ and $\{\omega_{\text{Alf}}\}_{\max}$ by cL and cR respectively.

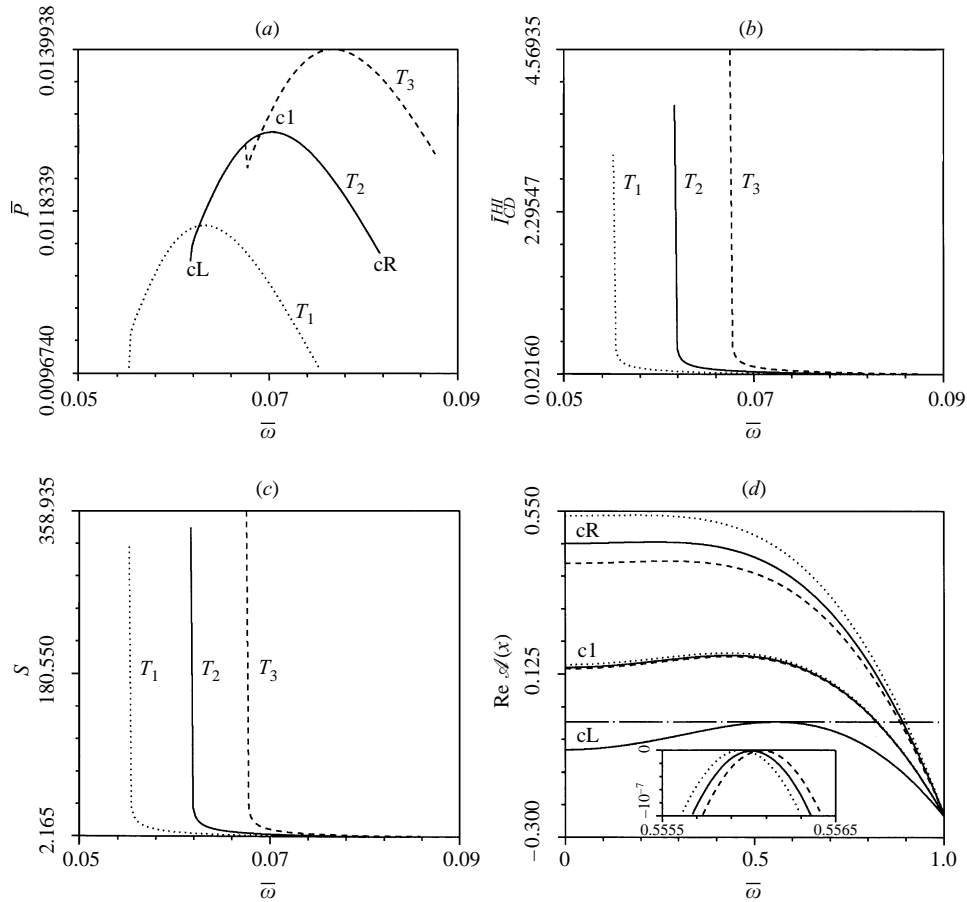


Figure 1. Frequency dependence of the total power absorption \bar{P} , (128) (a), total helicity-injection current drive \bar{I}_{CD}^{HI} , (125) (b), and efficiency $S = \bar{I}_{CD}^{HI}/\bar{P}$ (c), for three electrical-resistivity values corresponding to the temperatures $T_1 = 80$ eV, $T_2 = 100$ eV and $T_3 = 120$ eV. The symbols cL, c1 and cR indicate values corresponding to the lower edge, maximum power absorption and upper edge of the continuum Alfvén spectrum, respectively. (d) shows the radial profile of $\text{Re } \mathcal{A}$ (where \mathcal{A} is defined by (116)) for $\bar{\omega} = \bar{\omega}_{cL}$, $\bar{\omega}_{c1}$ and $\bar{\omega}_{cR}$ respectively.

cR is the same as in Fig. 1(a); the dotted, solid and dashed curves correspond to the temperatures T_1 , T_2 and T_3 . As can be seen, the curves have at least one zero; in the $\bar{\omega} = \bar{\omega}_{cL}$ case the two zeros coalesce, and the radial distances of the coalesced zeros are, within less than 10^{-10} , the same for all three temperatures.

A more detailed analysis of Fig. 1(a) shows that, in fact, in the domain $\bar{\omega} = \bar{\omega}_{cL} + \delta\bar{\omega}$ ($\delta\bar{\omega} \ll \bar{\omega}_{cL}$) additional resonant peaks in the power absorption do exist (see Fig. 2a). For example, in the case labelled T_2 , we find a sequence of peaks at $\bar{\omega}_{cL} < \bar{\omega}_{c3} < \bar{\omega}_{c2} (< \bar{\omega}_{c1})$. For completeness, in Figs 2(b–d) we show the $\bar{\omega}$ dependence of the HI current drive and efficiency corresponding to Fig. 2(a). Also, in Fig. 2(d) we plot the function $\text{Re } \mathcal{A}$ versus x for the three frequency values corresponding to the points labelled cL, c3 and c2 in Fig. 2(a).

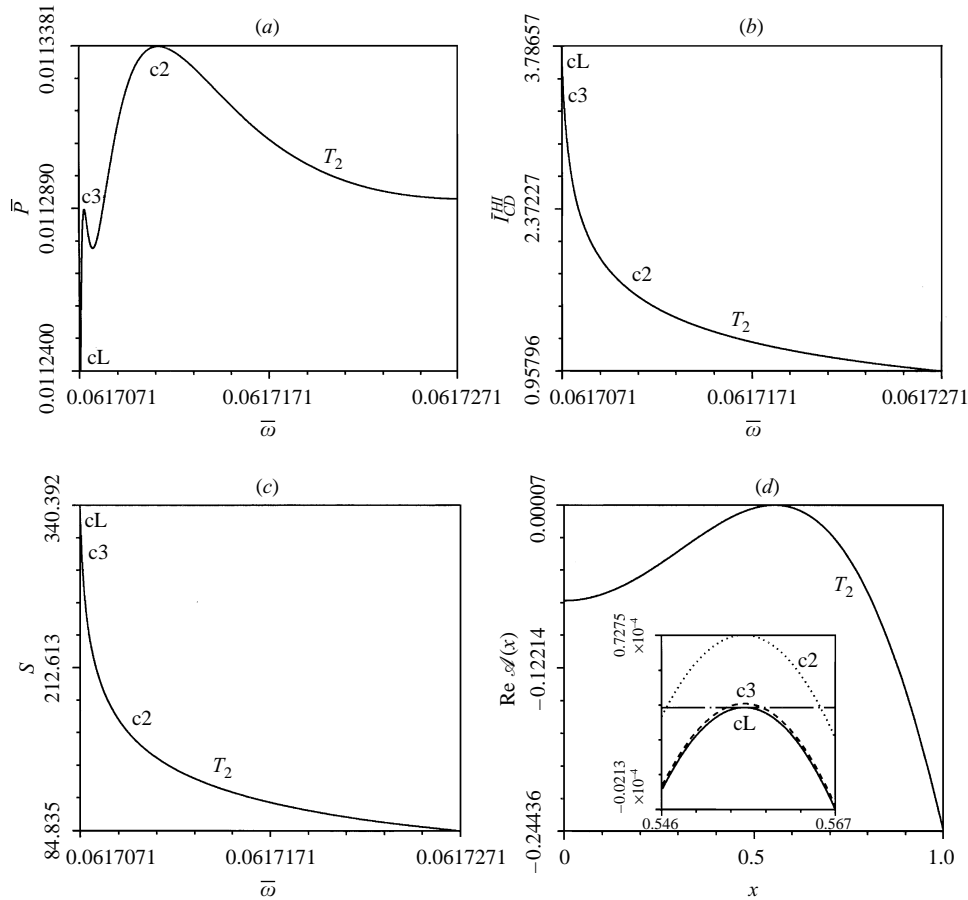


Figure 2. Enlargement of the frequency spectra for T_2 shown in Figs 1(a-d), in the domain $\bar{\omega} = \bar{\omega}_{cL} + \delta\bar{\omega}$, $\delta\bar{\omega} \ll \bar{\omega}_{cL}$ (for $\bar{\omega} = \bar{\omega}_{cL}$, $\bar{\omega}_{c3}$ and $\bar{\omega}_{c2}$).

7.1.2. *Radial profiles (localization) of the HI current drive.* For illustration, we present in Figs 3(a-c) the radial profiles of the HI current drive corresponding to the frequencies $\bar{\omega}_{cL}$, $\bar{\omega}_{c3}$ and $\bar{\omega}_{c2}$ defined in Fig. 2 (on the curve $P(T_2)$). Also, in Figs 4(a-c) we compare the radial profiles associated with the frequencies $\bar{\omega}_{cL}$, $\bar{\omega}_{c1}$ and $\bar{\omega}_{cR}$ corresponding to the three temperatures considered in Fig. 1. The results can be summarized as follows (see also Table 1).

- (i) For a given temperature (e.g. $T_2 = 100$ eV), the maximum HI current drive density $(j_{CD}^{HI})_{\max}$, increases significantly with frequency; on the other hand, the radial distance of $(j_{CD}^{HI})_{\max}$ changes only slightly with $\bar{\omega}$. Indeed, normalizing frequencies to ω_{cL} , currents to $[j_{CH}^{HI}(\bar{\omega}_{cL})]_{\max}$ and radial distances to that corresponding to $[j_{CH}^{HI}(\bar{\omega}_{cL})]_{\max}$ one finds the relative numbers shown in Table 2.
- (ii) Comparison of the results obtained for the three temperatures, $T_1 - T_3$, shows that (a) for each one of the frequencies $\bar{\omega}_{cL}$, $\bar{\omega}_{c1}$, and $\bar{\omega}_{cR}$, the maximum HI current drive density increases significantly with the temperature; and (b) the radial localization of the maximum current, while being almost the same at ω_{cL}

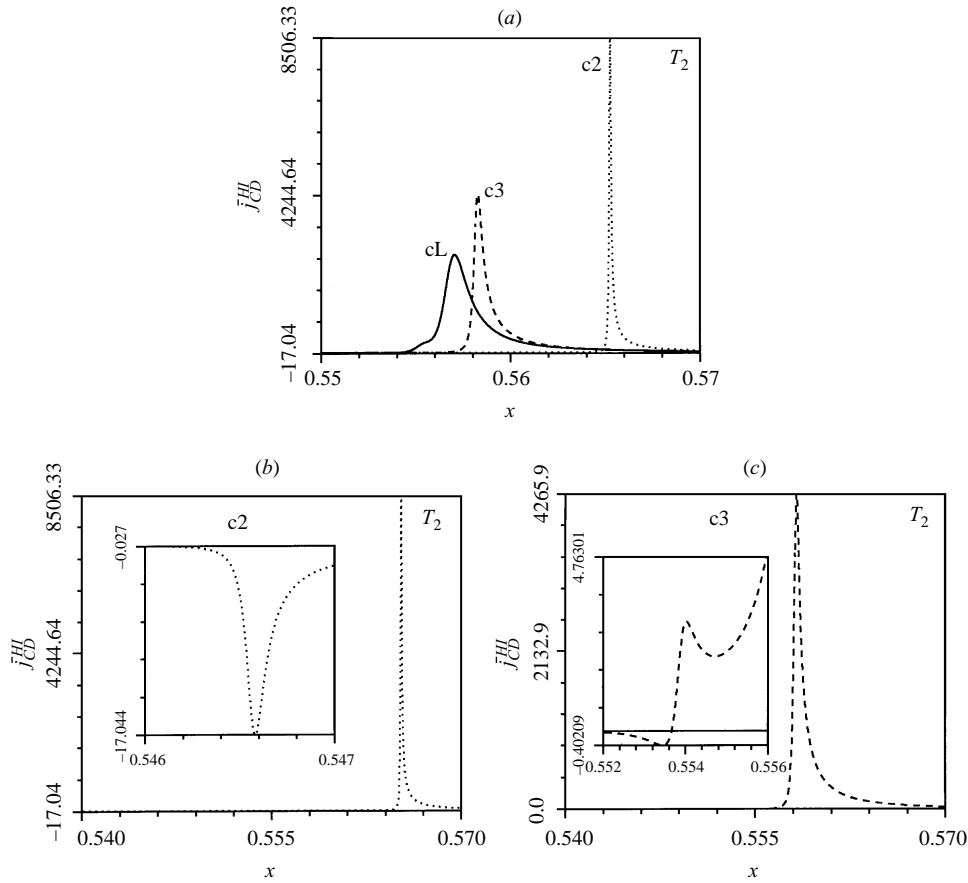


Figure 3. Radial profile of the HI current drive density, (122), corresponding to the frequency values $\bar{\omega}_{cL}$, $\bar{\omega}_{c3}$ and $\bar{\omega}_{c2}$.

(which is itself almost T -independent) decreases with increasing temperature that is clearly seen in Table 3.

7.1.3. *Structure of the EM wave field components.* Inspection of (119) for the HI current-drive density indicates that, all other parameters being fixed, j_{CD}^{HI} depends on the electrical resistivity $\eta_{\parallel} = \eta_{\parallel}(T)$ (120) in two ways:

- (a) directly through the term multiplying the expression in the curled brackets ($\sim 1/n\eta_{\parallel} \sim T^{3/2}/n$);
- (b) indirectly, through \mathbf{R}_{ei} (or equivalently through the quantity ν_{ei}/ω_{ce} , which affects the solutions of the wave equation).

Now, it is found that, in addition to the obvious increase with temperature due to the multiplying quantity, the value of the expression in the curly brackets also increases with temperature, consistent with the results in Figs 1–4. For illustration, we present in Figs 5(a–f) the radial profiles of the field components $\text{Re } E_{\perp}$ (left) and $\text{Im } E_{\perp}$ (right) obtained as a solution of the wave equation (108) for the same three temperature values indicated above; from top to bottom, $\bar{\omega} = \bar{\omega}_{cL}$ (a, d), $\bar{\omega} = \bar{\omega}_{c1}$

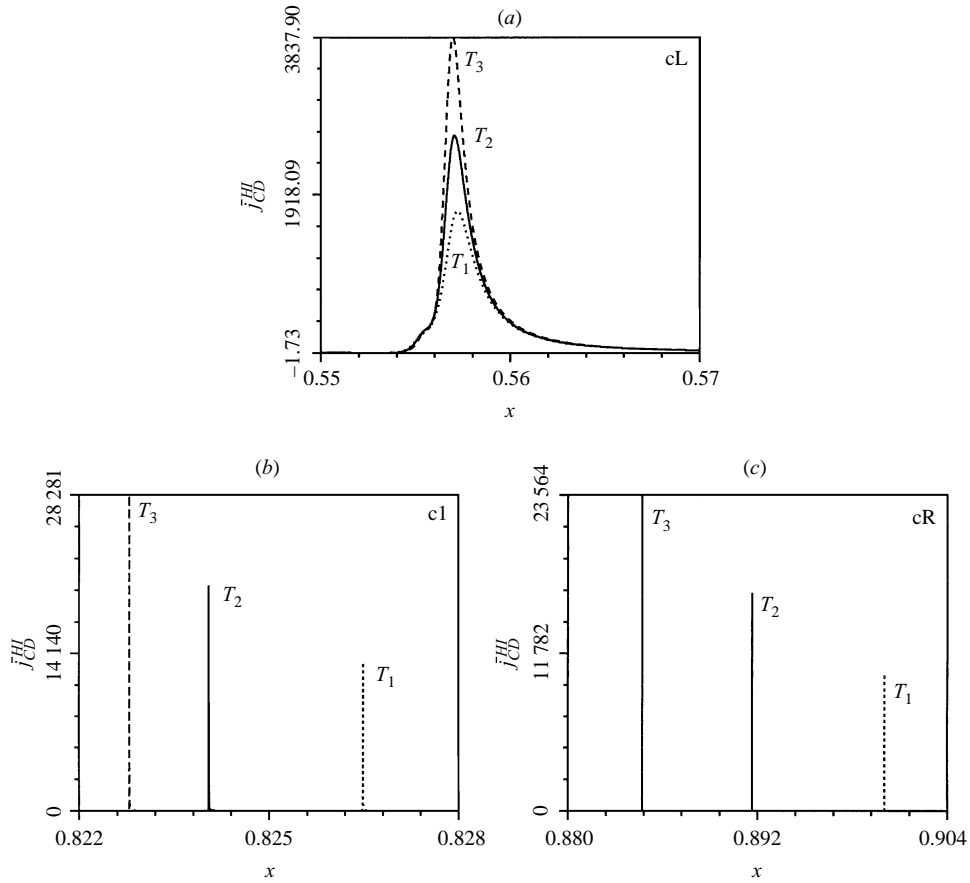


Figure 4. As Fig. 3, but for frequency values $\bar{\omega}_{cL}$ (a), $\bar{\omega}_{c1}$ (b) and $\bar{\omega}_{cR}$ (c).

Table 1. Maximum helicity-injection current drive and radial distance for four relevant normalized frequency values, namely $\bar{\omega}_{cL}$, $\bar{\omega}_{c3}$, $\bar{\omega}_{c2}$ and $\bar{\omega}_{c1}$ (lower edge of the continuum, closest peak, next-to-closest peak and maximum peak of the continuum respectively).

	T_1	T_2	T_3
$\bar{\omega}_{cL}$	0.055216	0.0617070	0.0675683
$(\bar{j}_{CD}^{HI})_{\max}$	1.717×10^3	2.645×10^3	3.837×10^3
$x[(\bar{j}_{CD}^{HI})_{\max}]$	0.55717	0.55699	0.55693
$\bar{\omega}_{c3}$	0.05521584	0.0617072	0.06756869
$(\bar{j}_{CD}^{HI})_{\max}$	2.679×10^3	4.265×10^3	6.751×10^3
$x[(\bar{j}_{CD}^{HI})_{\max}]$	0.55833	0.55825	0.55854
$\bar{\omega}_{c2}$	0.0552192	0.0617112	0.0675732
$(\bar{j}_{CD}^{HI})_{\max}$	5.259×10^3	8.506×10^3	1.256×10^4
$x[(\bar{j}_{CD}^{HI})_{\max}]$	0.56498	0.56523	0.56549
$\bar{\omega}_{c1}$	0.0632156	0.0703737	0.0769017
$(\bar{j}_{CD}^{HI})_{\max}$	1.3319×10^4	1.9563×10^4	2.8277×10^4
$x[(\bar{j}_{CD}^{HI})_{\max}]$	0.82648	0.82404	0.82279

Table 2. Relative frequency, maximum current drive and radial distance corresponding to the relevant frequency values $\bar{\omega}_{cL}$, $\bar{\omega}_{c3}$ and $\bar{\omega}_{c2}$ for $T = 100$ eV. Here $\bar{\omega}_i = \bar{\omega}_i/\bar{\omega}_{cL}$, $(\bar{J}_{CD}^{HI})_{\max} \equiv (\bar{J}_{CD,i}^{HI})_{\max}/(\bar{J}_{CD,cL}^{HI})_{\max}$ and $\bar{x} = x_i/x_{cL}$, where $i=c3, c2$.

	cL	c3	c2
$\bar{\omega}$	1	1.001	1.002
$(\bar{J}_{CD}^{HI})_{\max}$	1	1.5	2.0
$\bar{x}[(\bar{J}_{CD}^{HI})_{\max}]$	1	1.001	1.002

Table 3. As Table 2, but for $\bar{\omega}_{c1}$ (corresponding to maximum power absorption) and $\bar{\omega}_{cR}$ (upper edge of the continuum).

	cL			c1			cR		
	T_1	T_2	T_3	T_1	T_2	T_3	T_1	T_2	T_3
$\bar{\omega}$	0.8948	1.0	1.0949	1.0244	1.1404	1.2462	1.2189	1.3241	1.4191
$(\bar{J}_{CD}^{HI})_{\max}$	0.6493	1.0	1.4508	5.0352	7.6275	10.689	3.8633	6.1605	8.9071
$\bar{x}[(\bar{J}_{CD}^{HI})_{\max}]$	1.0003	1.0	0.9999	1.4838	1.4794	1.4772	1.6158	1.6008	1.5883

(*b, e*) and $\bar{\omega} = \bar{\omega}_{cR}$ (*c, f*). As can be seen, the basic features mentioned above, namely the increase in field amplitude and the shift towards smaller radial distances of its maximum value, are clearly demonstrated.

7.1.4. Scaling relations. Finally, to explore the range of validity of the results obtained so far, we have solved the problem for temperatures between 20 and 1000 eV. The results are presented in Figs 6(*a-c*). As can be clearly seen, the previous conclusions hold here as well. More specifically, the following scaling laws hold:

$$\begin{aligned} \bar{P}_{\max} &= 0.001\,687\bar{T}^{0.4378}, \\ (\bar{I}_{CD}^{HI})_{\max} &= 0.1037\bar{T}^{0.7854}, \\ S_{\max} &= 86.43\bar{T}^{0.3033}, \\ \bar{\omega}(S_{\max}) \approx \bar{\omega}_{cL} &= 0.006\,299\bar{T}^{0.4950}. \end{aligned}$$

7.2. Global Alfvén eigenmodes

7.2.1. Total power absorption. So far only the continuum range of the Alfvén-wave (CAW) spectrum has been considered (see Figs 1–6 and Tables 1–3). We now consider the discrete, global Alfvén eigenmodes (GAEs). A schematic representation of the full power-absorption spectrum (CR + DR) results is given in Fig. 7, for the three temperatures (i.e. resistivity values) used in Fig. 1 (top row, T_1 ; middle, T_2 ; bottom, T_3).

The following remarks hold:

- (i) for the given parameters, five discrete, very narrow peaks are shown to exist, namely, from left to right, G0 (the first radial mode) to G4 (the fifth radial mode);
- (ii) the frequencies corresponding to G0, . . . ,G4 accumulate below ω_{cL} ;
- (iii) the peak-power absorbed at these frequencies decreases strongly with G_i ($i = 0, 1, \dots, 4$): $\bar{P}(i) \gg \bar{P}(i + 1)$;

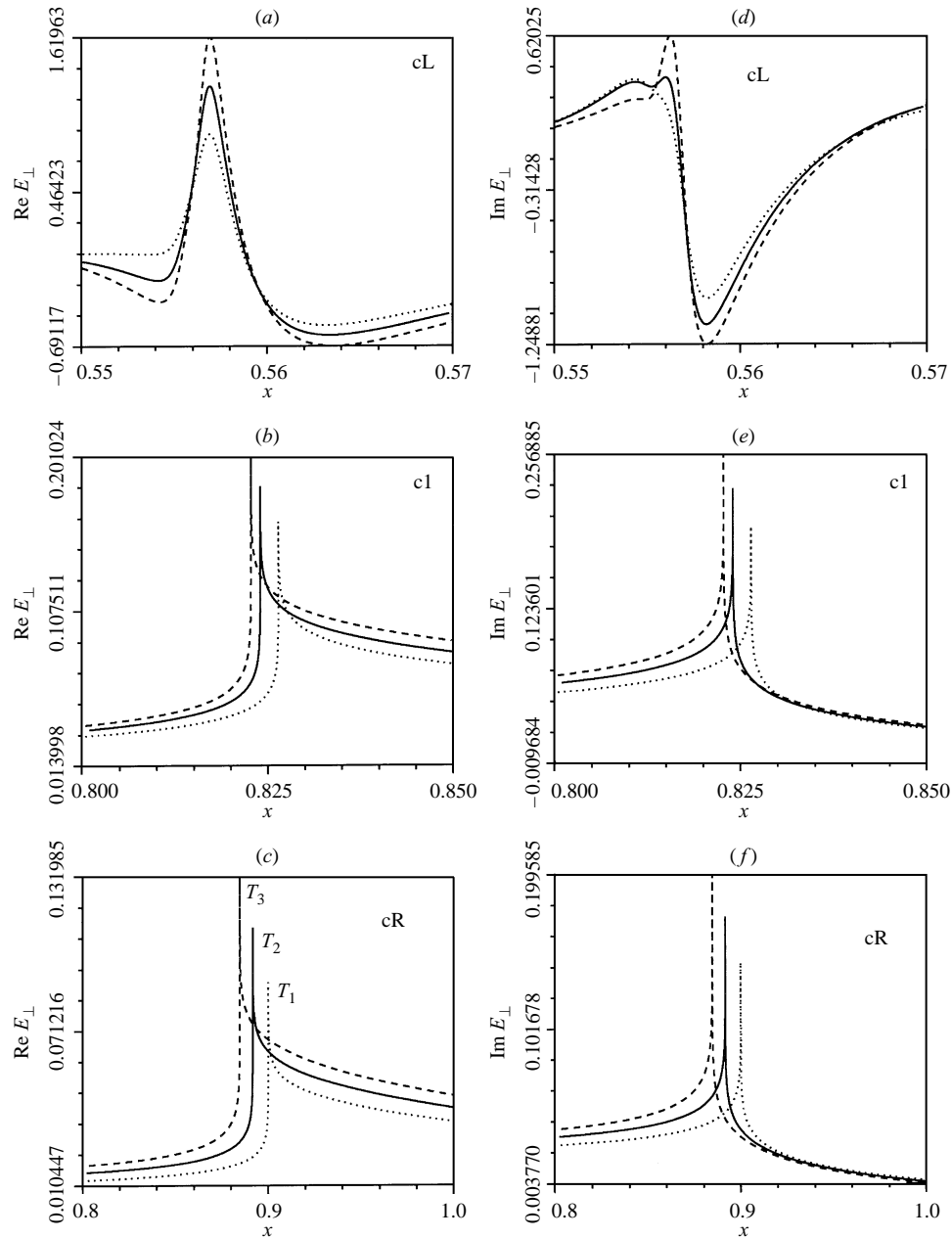


Figure 5. Solutions of the wave equation for the real (left) and imaginary (right) parts of the component E_{\perp} . From top to bottom: $\bar{\omega} = \bar{\omega}_{cL}$, $\bar{\omega} = \bar{\omega}_{c1}$ and $\bar{\omega} = \bar{\omega}_{cR}$ respectively. The dotted, solid and dashed curves correspond respectively to the temperatures T_1 , T_2 and T_3 indicated in Fig. 1.

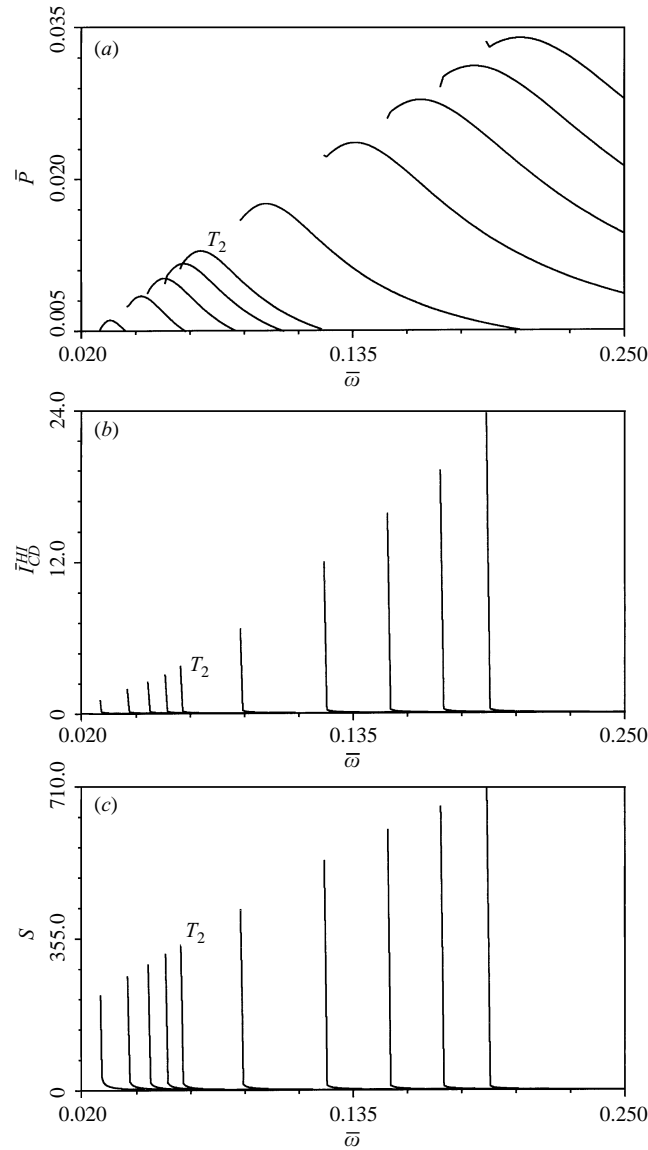


Figure 6. As Figs 1(a–c), but for the following sequence of temperatures (in eV): 20 (the first curve), 40, 60, 80, 100 (marked T_2), 200, 400, 600, 800 and 1000.

- (iv) however, even $\bar{P}_{\max}(4)$, which is the smallest in the DR range, is a factor of about 2.7 (T_1) to 6 (T_3) larger than the maximum power absorbed in the continuum range;
- (v) in all cases, the relative width of the peak, $\Delta\omega_i(\bar{P}_i = 0.5 \bar{P}_{i,\max})/\omega_i$, is infinitesimally small;
- (vi) increasing the temperature results in a significant increase of the maximum power absorption as well as in a shift towards higher values of the corresponding frequencies.

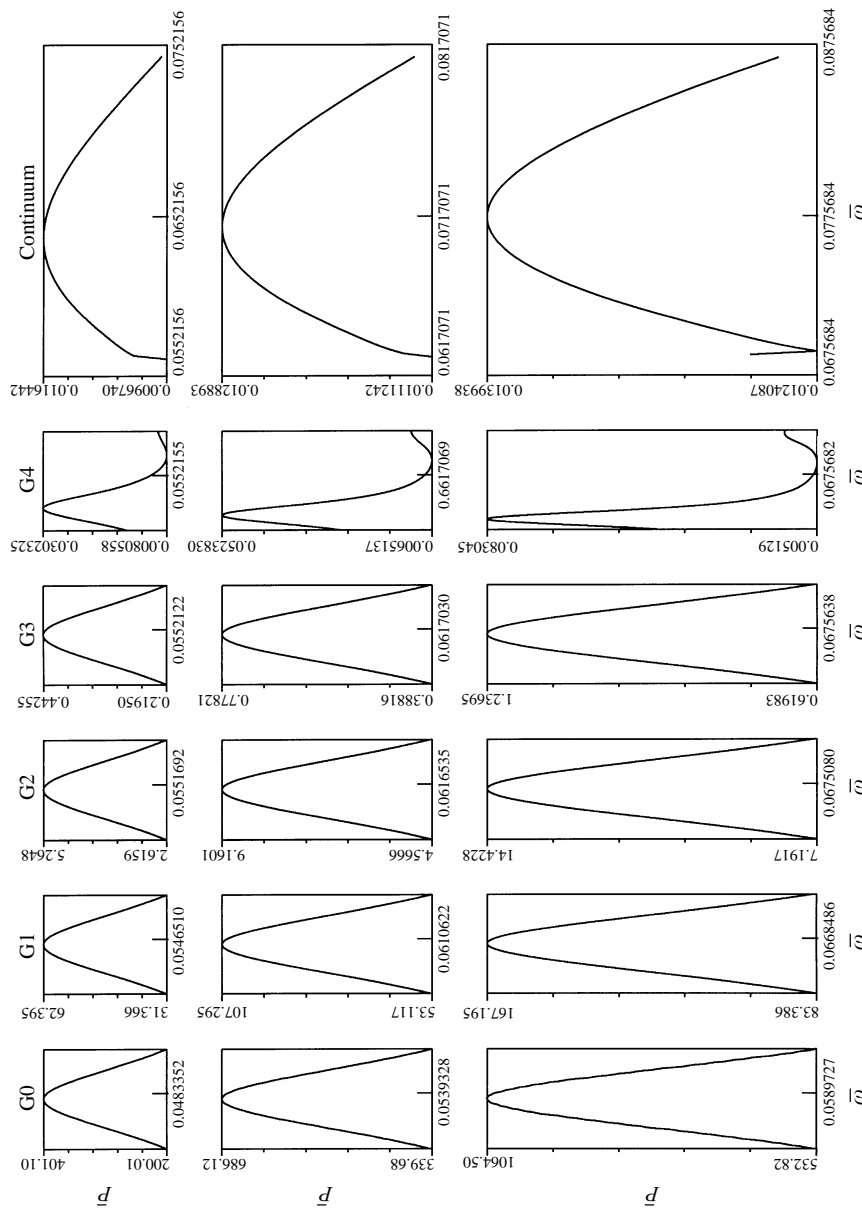


Figure 7. Comparative continuum and discrete frequency spectra of power absorption $\bar{P}(\omega)$ for the three temperatures T_1 , T_2 and T_3 (from top to bottom) indicated in the caption to Fig. 1.

Table 4. Illustrative residual relative frequencies $1 - \omega_i/\omega_{cL}$, total power absorption P_i/P_{cL} and width $\Delta\omega_{Gi}/\omega_{Gi}$ for the temperatures T_1 (80 eV), T_2 (100 eV) and T_3 (120 eV). Here, the illustrated GAEs are $i = 0, 2, 4$; ω_{c1} is the frequency corresponding to the maximum power absorption in the continuum; $\Delta\omega_{Gi}$ the width corresponding to half of the maximum P_{Gi} value.

	T_1	T_2	T_3
$1 - \omega_{G0}/\omega_{cL}$	0.1246	0.1260	0.1272
$P(\omega_{G0})/P_{cL}$	4.15×10^4	6.17×10^4	8.36×10^4
$\Delta\omega_{G0}/\omega_{G0}$	3.93×10^{-6}	2.56×10^{-6}	1.83×10^{-6}
$1 - \omega_{G2}/\omega_{cL}$	8.41×10^{-4}	8.69×10^{-4}	8.94×10^{-4}
$P(\omega_{G2})/P_{cL}$	8.23×10^1	5.44×10^2	1.23×10^3
$\Delta\omega_{G2}/\omega_{G2}$	2.50×10^{-6}	1.69×10^{-6}	1.21×10^{-6}
$1 - \omega_{G4}/\omega_{cL}$	4.45×10^{-6}	4.77×10^{-6}	4.96×10^{-6}
$P(\omega_{G4})/P_{cL}$	3.125	4.709	6.523
$\Delta\omega_{G4}/\omega_{G4}$	5.73×10^{-6}	5.61×10^{-6}	5.51×10^{-6}
$1 - \omega_{c1}/\omega_{cL}$	-0.145	-0.140	-0.138
$P(\omega_{c1})/P_{cL}$	1.204	1.159	1.099

7.2.2. *Total helicity injection current drive and efficiency.* Figures 8 and 9 show respectively the frequency dependences of \bar{I}_{CD}^{HI} and S corresponding to the GAEs $G0, \dots, G4$, for the temperatures T_1, T_2 and T_3 (top, middle and bottom rows, respectively). As can be seen (see Table 5),

- (i) like the power-absorption, the total HI current drive increases strongly with decreasing frequency value;
- (ii) in all cases, the GAE current values are much larger (or larger) than the continuum ones;
- (iii) the maximum GAE current values increase strongly with increasing temperature (i.e. with decreasing resistivity);
- (iv) unlike the continuum case, the total HI current values are almost symmetric functions of frequency; in the continuum case, they are very strongly decreasing with increasing frequency;
- (v) unlike the continuum case, the efficiency is almost constant over the entire frequency width of each GAE peak; it increases very strongly with the GAE rank, eventually reaching (about) the value of the maximum efficiency for the continuum: $S_0 < S_1 < S_2 < S_3 < S_4 \lesssim S_{cL}$.

7.2.3. *Localization of the HI current-drive density, j_{CD}^{HI} .* In Figs 10(a–e), the radial profiles $j_{CD}^{HI}(x)$ (119) are presented for the temperature values T_1, T_2 and T_3 (dotted, solid and dashed curves respectively). As can be seen,

- (i) for all $G0, \dots, G4$ modes, significant, mainly positive, HI current-drive density radial profiles are found;
- (ii) the values of the maximum current density increase very significantly with temperature, thus supporting the findings for the total current shown in Fig. 8;

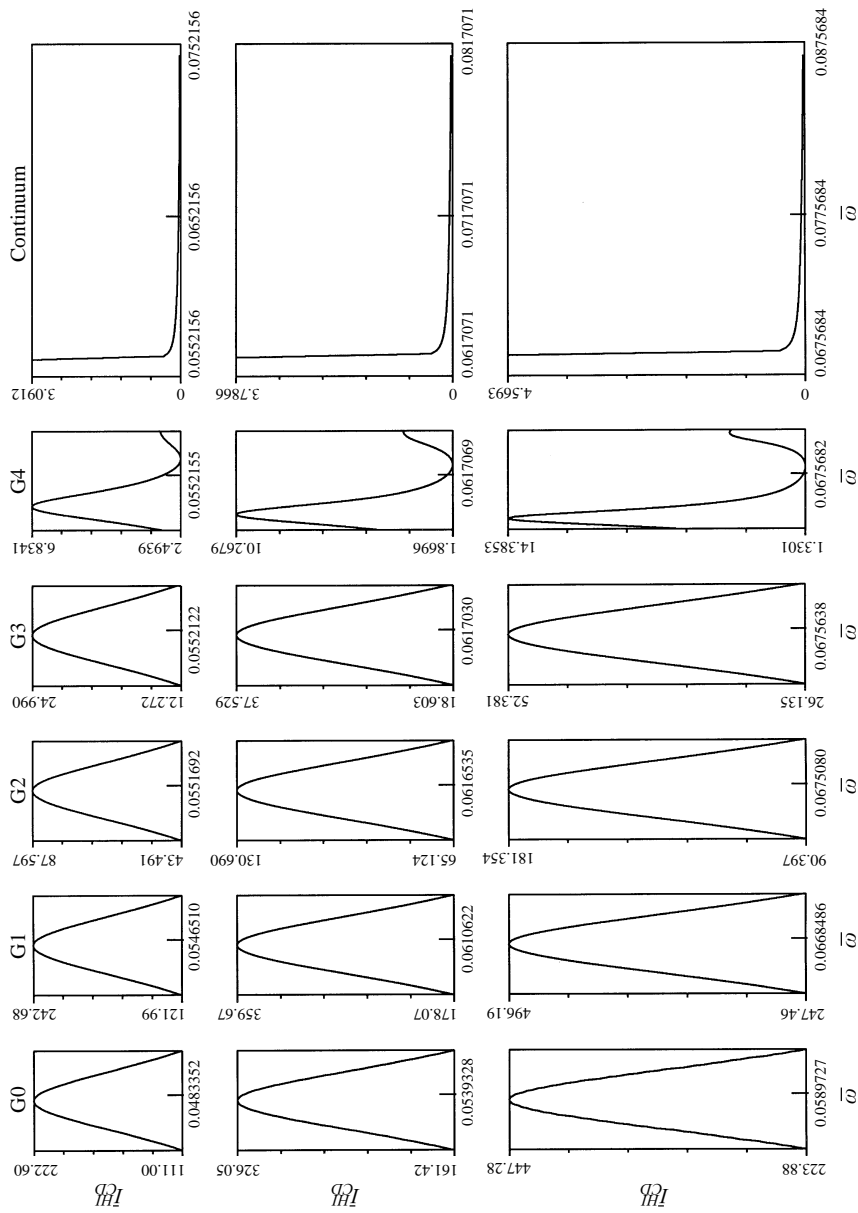


Figure 8. Total HI current-drive spectra corresponding to the five GAEs G0, . . . , G4 shown in Fig. 7.

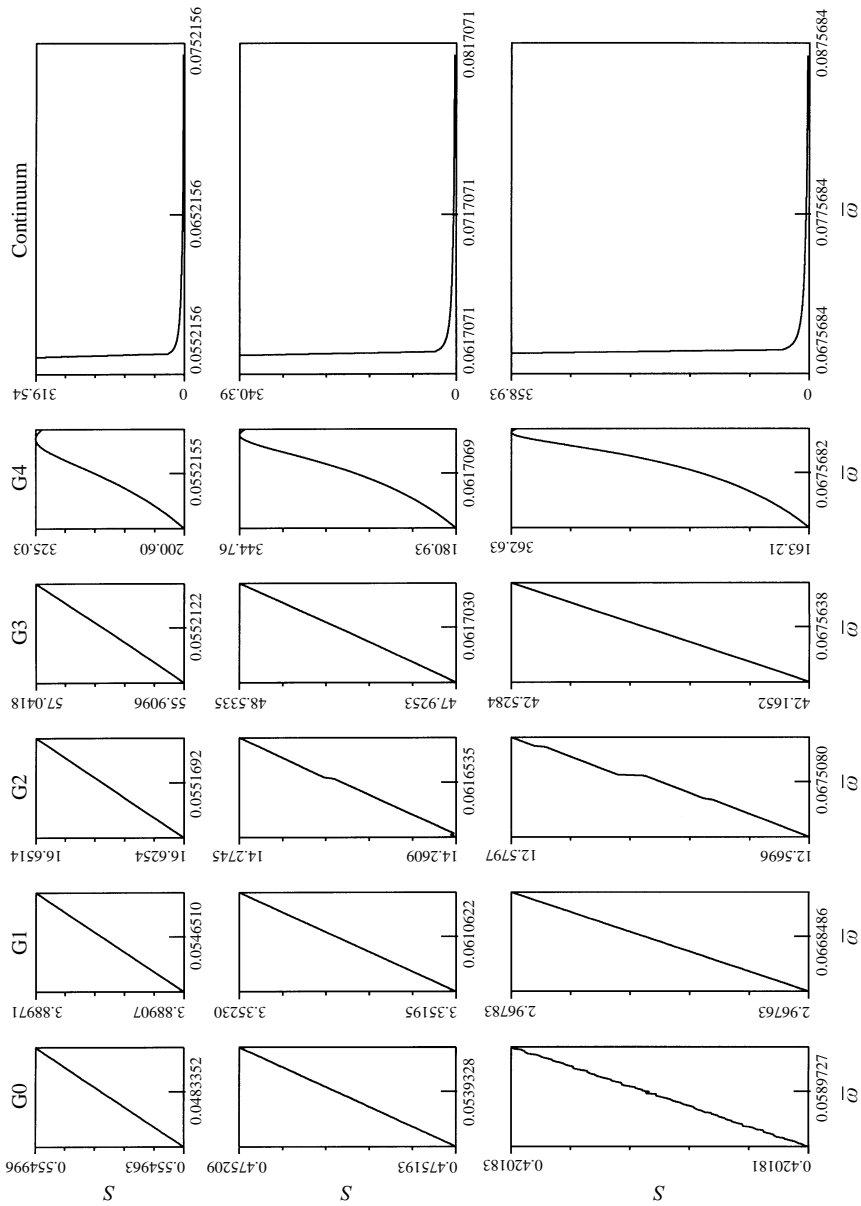


Figure 9. Efficiency of the HI current-drive spectra corresponding to the five GAEs G0, ..., G4 shown in Fig. 7.

Table 5. Total HI current drive \bar{I}_{CD}^{HI} and efficiency $S = \bar{I}_{CD}^{HI}/\bar{P}$ for several relevant frequency values and temperatures T_1 , T_2 and T_3 . Here $\bar{\omega}_i = \omega_i/\omega_{cL}$ and $\bar{S}_i = S_i/S_{cL}$ ($S_i \equiv I_i/P_{Gi}$ and $S_{cL} \equiv I_{cL}/P_{cL}$).

	T_1	T_2	T_3
$\bar{\omega}_{G0}$	4.834×10^{-2}	5.393×10^{-2}	5.897×10^{-2}
$I_{0,\max}/I_{cL}$	7.20×10^1	8.61×10^1	9.79×10^1
$S_{0,\max}$	0.555	0.475	0.420
$\bar{\omega}_{G2}$	5.517×10^{-2}	6.165×10^{-2}	6.751×10^{-2}
$I_{2,\max}/I_{cL}$	28.34	34.51	39.69
$S_{2,\max}$	1.66×10^1	1.43×10^2	1.26×10^1
$\bar{\omega}_{G4}$	5.522×10^{-2}	6.171×10^{-2}	6.757×10^{-2}
$I_{4,\max}/I_{cL}$	2.202	2.709	3.148
$S_{4,\max}$	225.2	195.8	173.2
$\bar{\omega}_{cL}$	5.522×10^{-2}	6.171×10^{-2}	6.757×10^{-2}
I_{cL}/I_{cL}	1	1	1
S_{cL}	319.5	340.4	358.9
$\bar{\omega}_{c1}$	6.322×10^{-2}	7.037×10^{-2}	7.690×10^{-2}
I_{c1}/I_{cL}	1.754×10^{-2}	1.465×10^{-2}	1.227×10^{-2}
S_{c1}	4.657	4.303	4.005

Table 6. Localization of the maximum HI current drive density for the modes G0, ..., G4.

	mode				
	G0	G1	G2	G3	G4
$x[(j_{CD}^{HI})_{max}]$					
(T_1)	0.698 878	0.609 020	0.562 471	0.561 328	0.556 450
(T_2)	0.636 792	0.610 020	0.562 985	0.561 544	0.556 506
(T_3)	0.697 018	0.611 435	0.563 645	0.562 017	0.556 541

(iii) the radial distance (from the axis $x = 0$) of the maximum current density, $x[(j_{CD}^{HI})_{max}]$, decreases with increasing mode rank, as is found also in the continuum-range case (see Fig. 4); this is shown in Table 6 (we recall that in the CR case, for the same temperatures, $x[(j_{CD}^{HI})_{max}]$ ranges between 0.826 and 0.8222, i.e. it is less centred).

7.2.4. Solutions of the wave equation. For completeness, in Fig. 11 we show the radial profiles of the field component $\text{Re}(E_{\perp})$ (left) and $\text{Im}(E_{\perp})$ (right) as obtained from the solution of (108), for the frequencies G0, ..., G4 indicated in Fig. 7; the dotted, solid and dashed curves correspond to the temperatures T_1 , T_2 and T_3 respectively.† Thus

- (i) the number of zeros of $\text{Re}(E_{\perp})$, which determines the rank of the mode Gi , is evident;

† For clarity, in Figs 11(a–e), only the interesting parts of the profiles are shown.

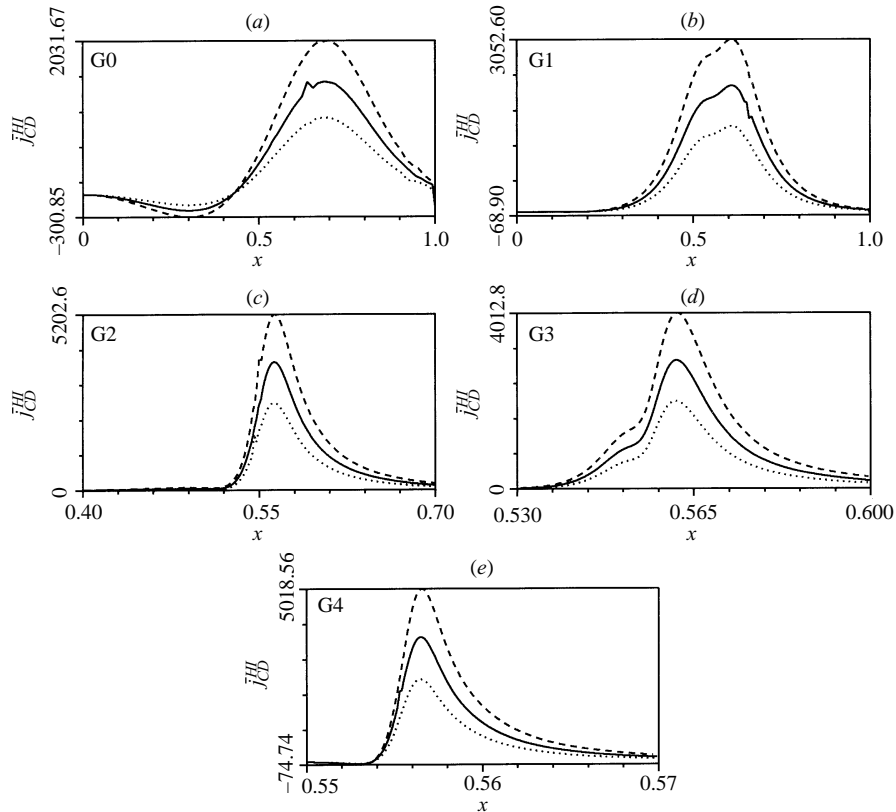


Figure 10. Radial profiles of the HI current-drive density corresponding to the five GAEs G0, . . . ,G4 shown in Fig. 7.

- (ii) the overall behaviour of the relative maximum intensity, structure and localization is such as to support the general features found for the power absorbed, current density and total current found and described above.

(Note that, in all cases, $\max|\text{Re}E_{\perp}| \gg \max|\text{Im}E_{\perp}|$).

Finally, in Fig. 12 we show the same information as in Fig. 11, for the field component E_N . Unlike the E_{\perp} -component, here the relation $\max|\text{Im}E_N| \gg \max|\text{Re}E_N|$ holds.

8. Summary

We have carried out a systematic investigation of resistive effects on the helicity-wave current drive generated by Alfvén waves in *simulated* tokamak plasmas.

For this purpose, a dielectric tensor appropriate for the physical conditions considered in this paper has been derived and presented. Both the *continuum range* (CR) and the *discrete range* (DR-GAE) have been considered.

The results of our combined analytical and computational investigation, illustrated in Figs 1–11 and Tables 1–6, reveal the following.

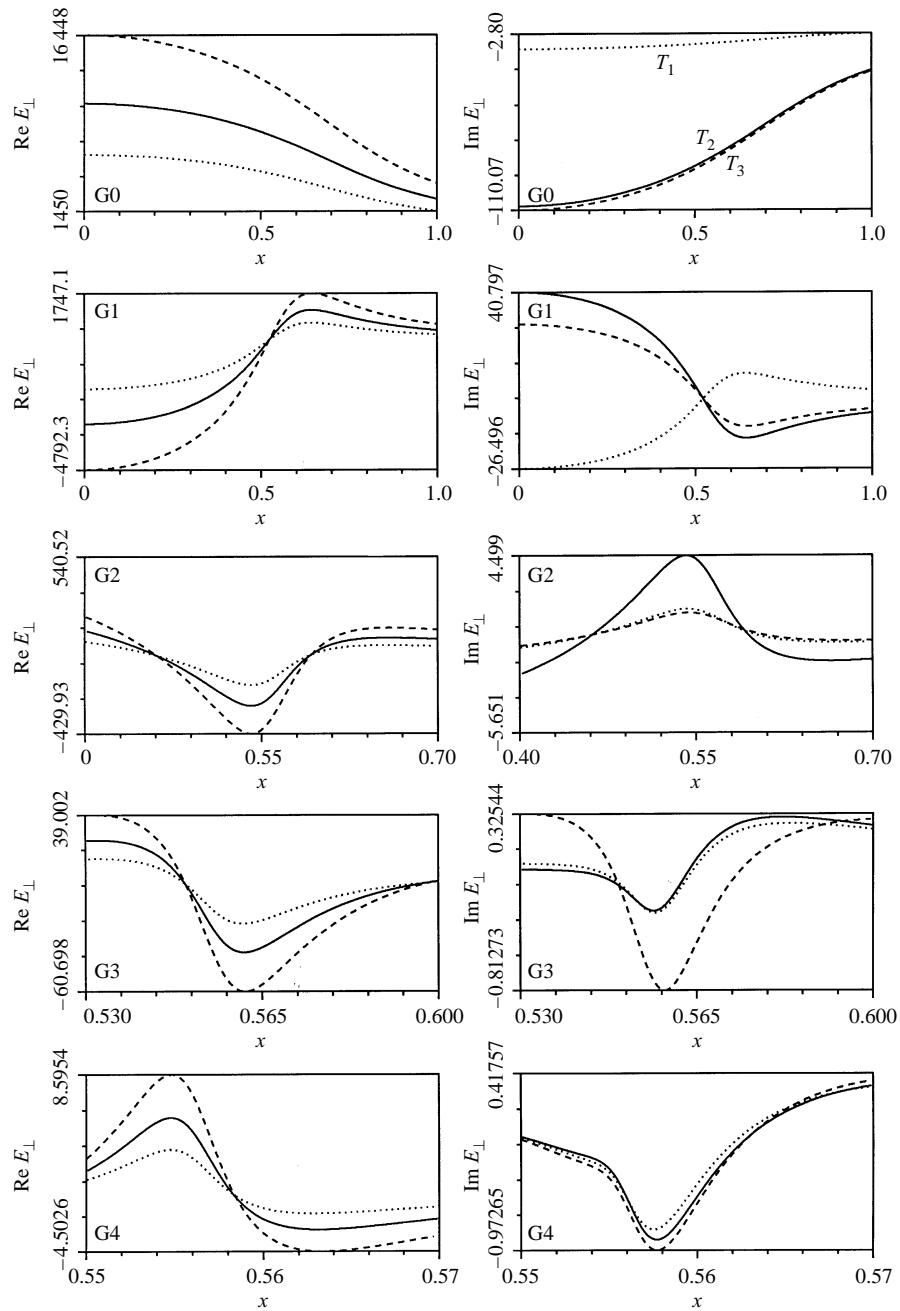


Figure 11. Solution of the wave equation for the real (left) and imaginary (right) parts of the component E_{\perp} . The radial profiles shown correspond respectively to the discrete modes G0, . . . , G4 belonging to the GAE spectrum. The dotted, solid and dashed curves correspond to the temperatures T_1 , T_2 and T_3 respectively.

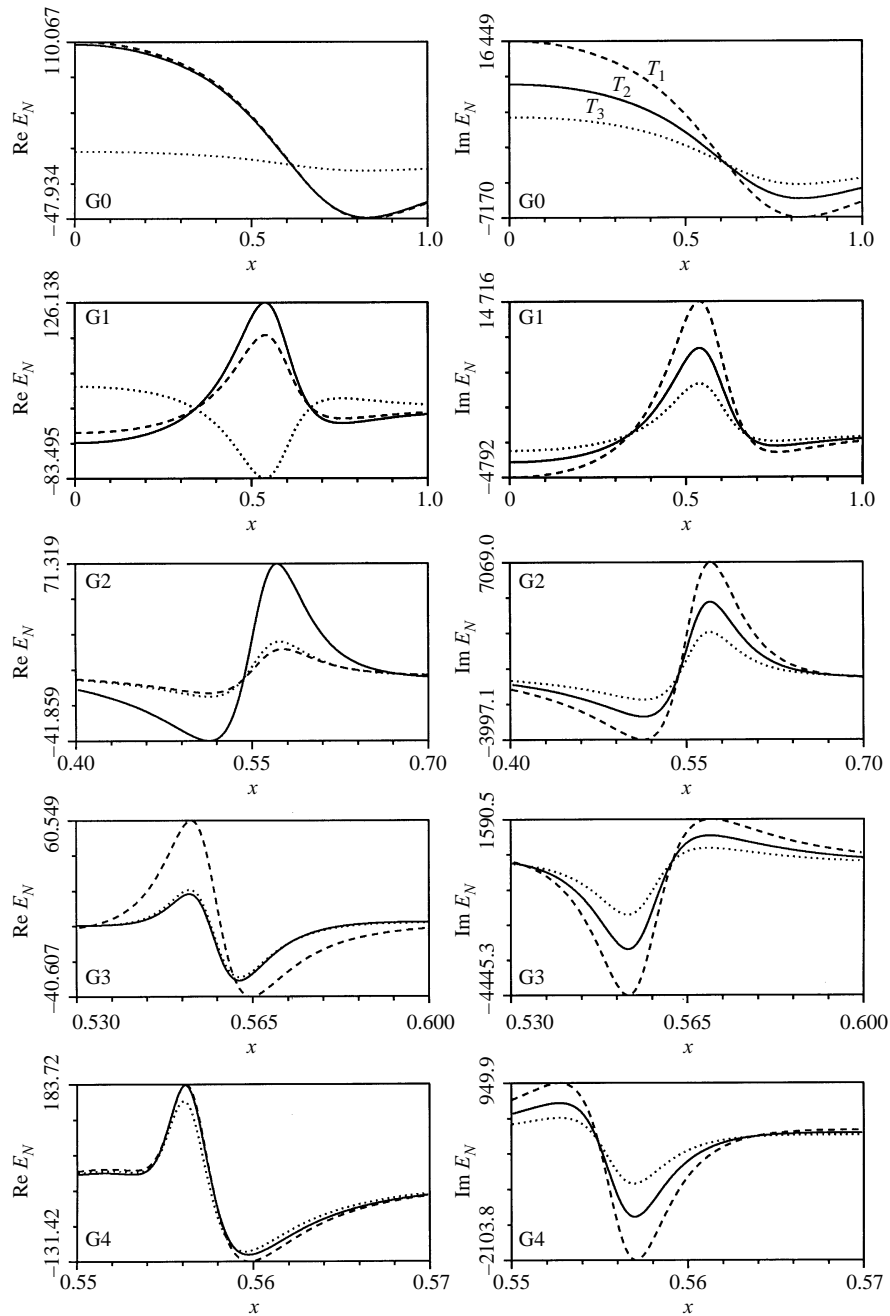


Figure 12. As in Fig. 11, but for the field component E_N .

Continuum range

- (i) The maximum power absorption as well the maximum helicity-injection current drive *increase significantly with decreasing resistivity* (i.e. with increasing temperature).

- (ii) Unlike the power absorption, which is a maximum at a frequency between the lower and the upper edge of the CR, the total current drive is a maximum at the lower edge, and decreases strongly with increasing frequency.
- (iii) The behaviour of the efficiency closely follows that of the current drive.
- (iv) The smaller the resistivity (i.e. the larger the temperature), the smaller is the radial distance from the axis ($x = 0$) of the maximum current-drive density.

Discrete range

- (i) The maximum power absorption in the discrete GAE case increases with decreasing resistivity even more strongly than in the CR case.
- (ii) Unlike the CR case, the total helicity-injection current has, for almost all GAEs, a symmetric frequency dependence about the line centre; its maximum value as well as the efficiency increase strongly with decreasing resistivity.
- (iii) Unlike the continuum case, the efficiency is almost constant over the entire width of the discrete mode; its value increases strongly with the GAE rank.
- (iv) Concerning the radial distance of the maximum current-drive density, the same general conclusions hold as for the CR case.
- (v) However, for the parameters considered here, this radial distance is about 50% smaller than in the CR case.

References

- Appert, K. and Václavík, J. 1983 *Plasma Phys.* **25**, 551.
- Appert, K., Gruber, R., Troyon, F. and Václavík, J. 1982 *Plasma Phys.* **24**, 1147.
- Braginskii, S. I. 1964 *Reviews of Plasma Physics*, Vol. 1 (ed. M. A. Leontovich), p. 205. Consultants Bureau, New York.
- Chan, V. S., Miller, R. L. and Ohkawa, T. 1990 *Phys. Fluids* **B2**, 1441.
- Cuperman, S., Bruma, C. and Komoshvili, K. 1996 *J. Plasma Phys.* **56**, 149.
- Elfimov, A. G., Petržílka, V. and Tataronis, J. A. 1994 *Phys. Plasmas*, **1**, 2882.
- Einaudi, G. and Mok, J. 1985 *J. Plasma Phys.* **34**, 259.
- Fukuyama, A., Itoh, K., Itoh, S.-I. and Hamamatsu, K. 1993 *Phys. Fluids* **B5**, 539.
- Hasegawa, A. and Chen, L. 1976 *Phys. Fluids* **19**, 1924.
- Kirov, A. G., Elfimov, A. G., Vojtenko D. A. *et al.* 1991 *Proceedings of International Conference on Plasma Physics and Controlled Nuclear Fusion Research, Washington*, Vol. 1, p. 831. IAEA, Vienna.
- Komoshvili, K., Cuperman, S. and Bruma, C. 1997 *J. Plasma Phys.* **57**, 611.
- Kulsrud, R. M. 1983 *Basic Plasma Physics I*, p. 115. North-Holland, Amsterdam.
- Mett, R. R. and Tataronis, J. A. 1990 *Phys. Fluids* **B2**, 2334.
- Mett, R. R. and Taylor, J. B. 1992 *Phys. Fluids* **B4**, 77.
- Mok, J. and Einaudi, G. 1985 *J. Plasma Phys.* **33**, 199.
- Ohkawa, T. 1989 *Comments Plasma Phys. Contr. Fusion* **12**, 165.
- Rauf, R. R. and Tataronis, J. A. 1996 *Phys. Plasmas*, **3**, 985.
- Shafranov, V. D. 1964 *Reviews of Plasma Physics*, Vol. 3 (ed. M. A. Leontovich), p. 4. Consultants Bureau, New York.
- Tataronis, J. A. 1975 *J. Plasma Phys.* **13**, 87.
- Tataronis, J. A. and Moroz, P. E. 1991 Helicity injection and fast wave current drive in scale tokamaks. *Proceedings of IAEA Technical Committee Meeting on Fast Current Drive in Reactor Scale Tokamaks, Arles, France*, p. 167. Association EURATOM-CEA.

Taylor, J. B. 1989 *Phys. Rev. Lett.* **63**, 1384.

Tsy-pin, V. S., Elfimov, A. G., de Azevedo, C. A. and de Assis, A. S. 1995 *Phys. Plasmas*, **2**, 2784.

Václavík, J. & Appert, K. 1991 *Nucl. Fusion* **31**, 1945.

Villard, L., Appert, K., Gruber R. and Václavík, J. 1986 *Comput. Phys. Rep.*, **4**, 95.

Wang, C. Y., Batchelor, D. B., Carter, M. D. *et al.* 1995 *Phys. Plasmas*, **2**, 2760.